AGU PUBLICATIONS

JGR

Journal of Geophysical Research: Solid Earth

RESEARCH ARTICLE
10.1002/2017JB014030

Key Points:
- The deeper locked-creeping fault transition can span a broad depth range, with distinct effective and geodetic locking depths
- The effective locking depth becomes shallower with time and relates to microseismicity at the bottom of the seismogenic zone
- The geodetic locking depth becomes deeper with time and relates to the potency release and depth extent of large earthquakes

Correspondence to:
J. Jiang,
junle@ucsd.edu

Citation:
Jiang, J., and N. Lapusta (2017), Connecting depth limits of interseismic locking, microseismicity, and large earthquakes in models of long-term fault slip, *J. Geophys. Res. Solid Earth*, *122*, 6491–6523, doi:10.1002/2017JB014030.

Received 25 JAN 2017
Accepted 14 JUL 2017
Accepted article online 20 JUL 2017
Published online 15 AUG 2017

Connecting depth limits of interseismic locking, microseismicity, and large earthquakes in models of long-term fault slip

Junle Jiang[1] **and Nadia Lapusta**[2]

[1]Institute of Geophysics and Planetary Physics, Scripps Institution of Oceanography, University of California, San Diego, La Jolla, California, USA, [2]Seismological Laboratory and Department of Mechanical and Civil Engineering, California Institute of Technology, Pasadena, California, USA

Abstract Thickness of the seismogenic zone is commonly determined based on the depth of microseismicity or the fault locking depth inferred from geodetic observations. The relation between the two estimates and their connection to the depth limit of large earthquakes remain elusive. Here we explore the seismic and geodetic observables in models of faults governed by laboratory-based friction laws that combine quasi-static rate-and-state friction and enhanced dynamic weakening. Our models suggest that the transition between the locked and fully creeping regions can occur over a broad depth range. The effective locking depth, D_{elock}, associated with concentrated loading and promoting microseismicity, is located at the top of this transition zone; the geodetic locking depth, D_{glock}, inverted from surface geodetic observations, corresponds to the depth of fault creeping with approximately half of the long-term rate. Following large earthquakes, D_{elock} either stays unchanged or becomes shallower due to creep penetrating into the shallower locked areas, whereas D_{glock} deepens as the slip deficit region expands, compensating for the afterslip. As the result, the two locking depths diverge in the late interseismic period, consistent with available seismic and geodetic observations from several major fault segments in Southern California. We find that D_{glock} provides a bound on the depth limit of large earthquakes in our models. However, the assumed layered distribution of fault friction and simple depth estimates are insufficient to characterize more heterogeneous faults, e.g., ones with significant along-strike variations. Improved observations and models are needed to illuminate physical properties and seismic potential of fault zones.

1. Introduction

Modern seismic and geodetic observations from major continental fault systems enable refined imaging of the crustal faulting process. Characteristics of large earthquakes and associated postseismic fault zone behavior are now routinely studied [e.g., *Reilinger et al.*, 2000; *Bouchon et al.*, 2002; *Simons et al.*, 2002; *Eberhart-Phillips et al.*, 2003; *Fialko et al.*, 2005; *Johnson et al.*, 2009], but monitoring of major faults is more commonly confined to their interseismic periods. Historical and paleoseismic records of past earthquakes and current interseismic observations thus comprise the critical information for understanding future events. In Southern California, assessing seismic risks of potential large earthquakes in the San Andreas Fault System poses a societal and scientific challenge (Figure 1). The 1857 M_{w} 7.9 Fort Tejon earthquake is the most recent major event on the southern San Andreas fault, which ruptured through the Cholame, Carrizo, and Mojave segments [*Sieh*, 1978; *Grant and Donnellan*, 1994; *Runnerstrom et al.*, 2002; *Zielke et al.*, 2010]. To the south, San Andreas fault segments were last ruptured around 1690 [*Sieh and Williams*, 1990; *Philibosian et al.*, 2011]. Geodetic observations of surface strain accumulation suggest that the southern San Andreas fault may be approaching the end of its interseismic period [*Fialko*, 2006]. In contrast, earthquakes of smaller magnitudes (M_{w} 6–7) struck the San Jacinto fault more frequently, resulting in a total of 9 events over the past 120 years [*Kagan et al.*, 2006; *Rockwell et al.*, 2015; *Onderdonk et al.*, 2015]. While the last major event of M_{w} 6.8 occurred on the southernmost section in 1968 [*Toppozada and Branum*, 2002], the Anza segment has not ruptured for about 200 years and awaits a major event of regional seismic impact.

Seismic and geodetic approaches have been used to provide independent estimates on the thickness of the seismogenic zone on faults [*Smith-Konter et al.*, 2011]. In Southern California, microseismicity patterns are

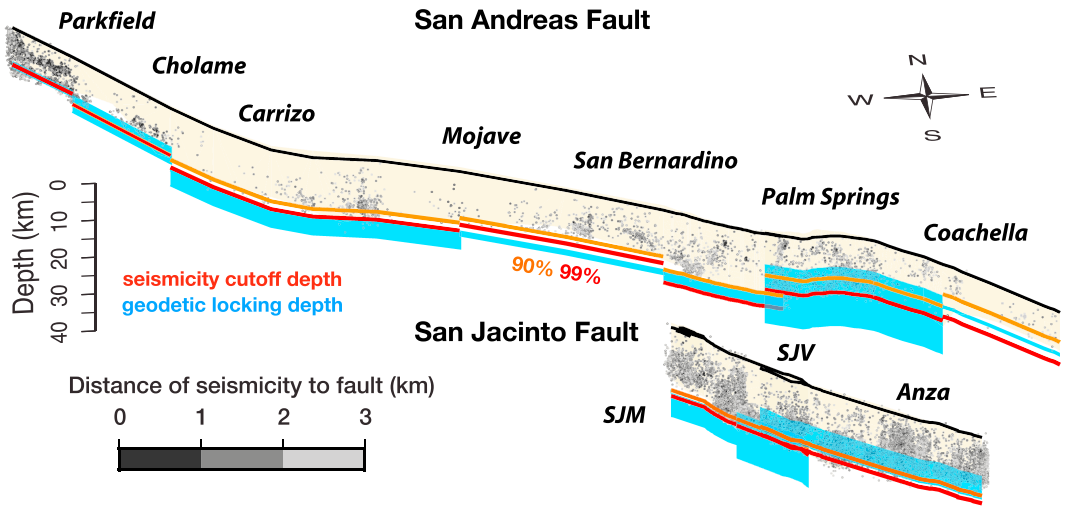

Figure 1. Microseismicity and geodetic locking depths on the San Andreas and San Jacinto faults in Southern California. The fault geometry is visualized in three dimensions based on the Community Fault Model for Southern California [*Plesch et al.*, 2007]. Blue bands indicate the one standard deviation (1σ) uncertainty range of fault locking depths estimated from surface geodetic measurements [*Smith-Konter et al.*, 2011]. Microseismicity that occurred within 3 km of the fault planes between 1981 and 2011 [*Waldhauser and Schaff*, 2008; *Hauksson et al.*, 2012] is represented by dots colored by their distance to the fault plane. Orange and red lines denote the 90% and 99% cutoff depths of seismicity [*Nazareth and Hauksson*, 2004; *Lin et al.*, 2007]. SJM: San Jacinto Mountain. SJV: San Jacinto Valley.

depth dependent and highly variable across fault segments (Figure 1). The spatial distribution of microseismicity is often used to define the base of the seismogenic zone by cutoff depths (D_{seis}), i.e., the depths above which a certain percentage (e.g., 90%, 95%, or 99%) of the seismicity occurs [*Nazareth and Hauksson*, 2004; *Lin et al.*, 2007]. Meanwhile, geodetic observations of surface strain accumulation across the fault are interpreted in terms of the depth of fault locking, often envisioned as the boundary between the locked and creeping regions of faults [e.g., *Savage and Burford*, 1973; *Smith-Konter et al.*, 2011]. These estimates are used to calculate the potency deficit expected to be released by future earthquakes, and hence, they are directly relevant to the assessment of regional seismic hazard. The effectiveness of such a practice depends on how well the seismic and geodetic estimates on interseismic faults reflect the depth extent of large earthquakes (D_{rupt}). Fundamentally, predicting the behavior of seismogenic faults requires a physical understanding of how various fault slip phenomena, including interseismic locking, microseismicity, and large earthquakes, interconnect over the depth range of faults and across multiple time scales.

The depths of fault locking and creeping play critical roles in physical models that aim to understand and reproduce long-term tectonic motion at plate boundaries [*Segall*, 2010]. The pioneering work of *Savage and Burford* [1973] considered deep creep on an infinitely long vertical strike-slip fault as a buried screw dislocation embedded in a homogeneous, linear elastic half-space, to model the interseismic surface deformation of the San Andreas fault. This two-dimensional (2-D) model assumes that the fault is fully locked above the depth of dislocation tip D, with a uniform creeping rate V_{cr} extending from the dislocation tip to infinite depth, and predicts that the along-strike surface velocity v is an arctangent function of the fault-normal distance x:

$$v(x) = \frac{V_{cr}}{\pi} \arctan \frac{x}{D}. \tag{1}$$

Due to its simple and analytic form, the elastic dislocation model has been widely used to interpret interseismic surface geodetic observations in terms of locking depths on faults. We call this estimate the "geodetic locking depth" (D_{glock}), unless specified otherwise. In this model, since the earthquake slip and interseismic creep occur exclusively within and below the seismogenic zone, respectively, the geodetic locking depth (D_{glock}) coincides with the depth extent of large earthquakes (D_{rupt}) (Figure 2). As a result of approximating slip as a uniform dislocation, infinite stresses arise at the dislocation tip.

Moving forward, models of seismic cycles were developed to reproduce the time dependence in geodetic observations. The term "seismic cycles" is used here to indicate sequences of earthquakes and aseismic deformation in between, not necessarily periodic or regular. Coupling of faults in an elastic lithosphere

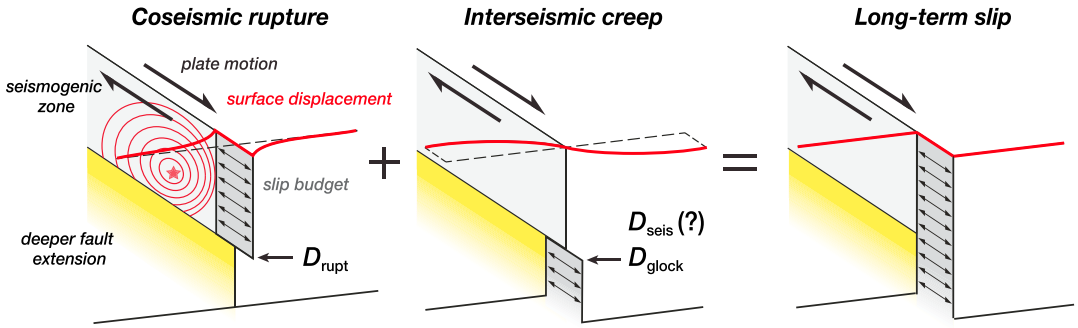

Figure 2. The conventional elastic dislocation model for the seismic cycle [*Savage and Burford*, 1973]. (right) The long-term fault slip budget comprises (left) coseismic earthquake slip and (middle) interseismic creep. In this model, coseismic fault slip is uniform with depth (indicated by arrows in the dark grey region) in the seismogenic zone (light gray) during large earthquakes (hypocenter as the red star and coseismic rupture fronts in contours), whereas interseismic creep occurs uniformly directly below on the deeper fault extension (yellow). The depth extent of large earthquake rupture, D_{rupt}, and the interseismic geodetic locking depth, D_{glock}, thus coincide at the base of the seismogenic zone. Microseismicity is not considered in such kinematic models, though it is often assumed that certain cutoff depths of microseismicity, D_{seis}, delineate the base of the seismogenic zone and thus are approximately the same as D_{glock}.

with a viscoelastic substrate in the context of seismic cycles was first introduced by *Savage and Prescott* [1978], building on the work of *Nur and Mavko* [1974]. More advanced numerical models were able to tackle three-dimensional problems with complex fault geometry [e.g., *Smith and Sandwell*, 2006] and include stress-controlled fault creep by considering more realistic stressing [e.g., *Li and Rice*, 1987; *Johnson and Segall*, 2004] or laboratory constitutive laws such as rate-and-state fault friction or inelastic bulk rheology [e.g., *Johnson and Segall*, 2004; *Smith and Sandwell*, 2004; *Hetland et al.*, 2010; *Takeuchi and Fialko*, 2012; *DeVries and Meade*, 2016]. With the coseismic ruptures approximated as imposed instantaneous slip confined to the seismogenic zone, these models typically focus on the postseismic and interseismic responses of the fault zone between large earthquakes. The surface deformation predicted by more sophisticated models can often be reproduced by the elastic dislocation model with time-dependent slip rates and locking depths [e.g., *Savage*, 1990; *Meade and Hager*, 2004; *Takeuchi and Fialko*, 2013], which serve as convenient kinematic parameters for characterizing interseismic geodetic observables of these models.

Among various constitutive relations, the rate- and state-dependent friction laws, empirically derived for fault resistance at low slip rates (10^{-9}–10^{-2} m/s) [*Dieterich*, 1979, 1981; *Ruina*, 1983], provide a unified explanation for a wide range of seismic cycle phenomena, including earthquake initiation, postseismic transients, aftershocks, and interseismic fault creep [*Dieterich*, 2007]. Such friction laws form the basis of an internally consistent framework for simulating earthquake sequences and aseismic slip [*Tse and Rice*, 1986; *Lapusta et al.*, 2000; *Lapusta and Liu*, 2009]. Models of rate-and-state faults are able to resolve spontaneous nucleation and rupture of earthquakes, as well as aseismic slip, in great detail, bridging observations over a range of time scales. Some recent models were adopted to understand earthquake patterns and interseismic coupling in subduction zones [*Kaneko et al.*, 2010] and tailored to reproduce the Parkfield earthquake sequence on the San Andreas fault [*Barbot et al.*, 2012].

Several important questions on seismogenic fault behavior remain to be explored, including incorporating sophisticated constitutive laws, considering complex fault slip scenarios, and integrating diverse observations. First, standard rate-and-state friction models are not fully consistent with our current laboratory-based understanding of dynamic fault friction. Over the recent decade, enhanced dynamic weakening of fault materials has been ubiquitously documented in laboratory friction experiments at high slip rates (~0.1 m/s and higher) [e.g., *Rice*, 2006; *Di Toro et al.*, 2011; *Tullis*, 2015, and references therein]. This mechanism, e.g., in the form of thermal pressurization, has been suggested to play an important role in earthquakes and long-term fault slip [e.g., *Sibson*, 1973; *Noda and Shimamoto*, 2005; *Rice*, 2006; *Noda and Lapusta*, 2013; *Cubas et al.*, 2015; *Viesca and Garagash*, 2015]. Understanding how models based on a full range of laboratory-based rock behavior connect with geophysical observations is critical for validations of laboratory laws and fundamental understanding of the observed phenomena.

Second, aseismic and seismic slip on faults can overlap in space and time. For example, the base of the seismogenic zone supports both the quasi-static nucleation and dynamic rupture of earthquakes [*Das and Scholz*, 1983; *Lapusta and Rice*, 2003]. Conventional models assume that earthquakes and fault creep occur on nearby fault areas, simply associated with velocity-weakening and velocity-strengthening rate-and-state friction, respectively. Relaxing such assumptions and exploring more general models may improve or change our interpretations of observations.

Third, microseismicity is largely not considered in models that focus on large-scale and/or long-term observations. While spatiotemporal complexity and interaction of spontaneous microseismicity have been studied in models that feature nonlinear dynamics [*Ben-Zion and Rice*, 1995; *Shaw and Rice*, 2000; *Lyakhovsky et al.*, 2001] or fault heterogeneity [*Hillers et al.*, 2006; *Dublanchet et al.*, 2013] (often ignoring slow tectonic loading and/or dynamic wave effects), the link between spatiotemporal microseismic behavior and geodetic observations is still largely missing. Presumably, small crustal earthquakes are strongly influenced by fault friction and rheology, as well as large-scale fault slip process [*Sibson*, 1982], therefore bearing important information about the state of seismogenic zone.

To start exploring these questions, *Jiang and Lapusta* [2016] simulated microseismicity and large earthquakes in models of faults that obey laboratory-based laws for both quasi-static and dynamic friction and incorporate simple fault heterogeneity. By comparing modeling results with observations, their study revealed how the depth extent of large earthquakes influences microseismicity, attributing the seismic quiescence on many major strike-slip faults to earthquake slip that penetrates below the traditionally defined seismogenic zone. *Jiang and Lapusta* [2016] demonstrated that such deeper slip leads to an updip migration of interseismic locked-creeping boundary, noting the association of this boundary with the highest loading and its distinction from the conventional geodetic locking depth. Qualitatively, larger geodetic locking depths (D_{glock}), e.g., on the Carrizo segment of the San Andreas fault [*Meade*, 2005; *Smith-Konter et al.*, 2011], are consistent with the inferred deeper coseismic slip on the fault. However, the relation of the conventional simplified notion of the geodetic locking depth to situations with large overlapping areas of seismic and aseismic slip is not clear. Hence, it is also not clear how the geodetic observations can be integrated with seismic observations to constrain the depth extent of large earthquakes on a particular fault segment.

In this study, we focus on understanding both seismic and geodetic observables arising in models of heterogeneous faults obeying laboratory friction laws, with the goal of connecting the depth limits of microseismicity, interseismic fault locking, and large earthquakes. These problems are explored in fault models with layered distributions of frictional properties, building upon the models of *Jiang and Lapusta* [2016]. The results and predictions of our models are then validated against the available observations from the San Andreas fault in Southern California, considering potential sources of bias and uncertainty, such as heterogeneity in elastic structure, three-dimensional (3-D) effects, and inelastic processes. Finally, we discuss additional scenarios in which fault heterogeneity, in the form of along-strike variations in the depth dependence of frictional properties, can complicate the various depth estimates, and how future observations can be improved to advance our understanding of deep fault zone properties.

In our simulations, we assume that the fault zone response predominantly results from frictional fault slip in a purely elastic bulk. This assumption holds well for the highly localized fault zone [e.g., *Chester and Chester*, 1998] in the brittle, elastic upper crust. Here we assume that this assumption reasonably describes fault behavior over a certain depth range below the traditionally defined seismogenic zones, at least for mature faults, since the existence of such localized deeper fault extensions is supported by nonvolcanic tremors [*Shelly*, 2010], deep afterslip [*Reilinger et al.*, 2000; *Bruhat et al.*, 2011], exhumed faults [*Cole et al.*, 2007], seismic tomography [*Henstock et al.*, 1997; *Parsons*, 1998; *Zhu*, 2000], and numerical models of ductile fault roots [*Takeuchi and Fialko*, 2012]. Although bulk stress relaxation is ignored at greater fault depths, the friction-based models allow us to start exploring the qualitative relation between seismic and geodetic observables. Our findings can then inform future modeling where the laboratory-based on-fault treatment is combined with inelasticity of the deeper crust.

2. Numerical Models of Faults

In our models, a 2-D planar strike-slip fault is embedded into a 3-D uniform linear elastic half-space (Figure 3a). The fault plane extends to the free surface at the top and is prescribed with a fixed plate loading rate, V_{pl}, at the bottom. On the fault, we adopt the commonly used standard rate-and-state friction (RSF) law, with the aging

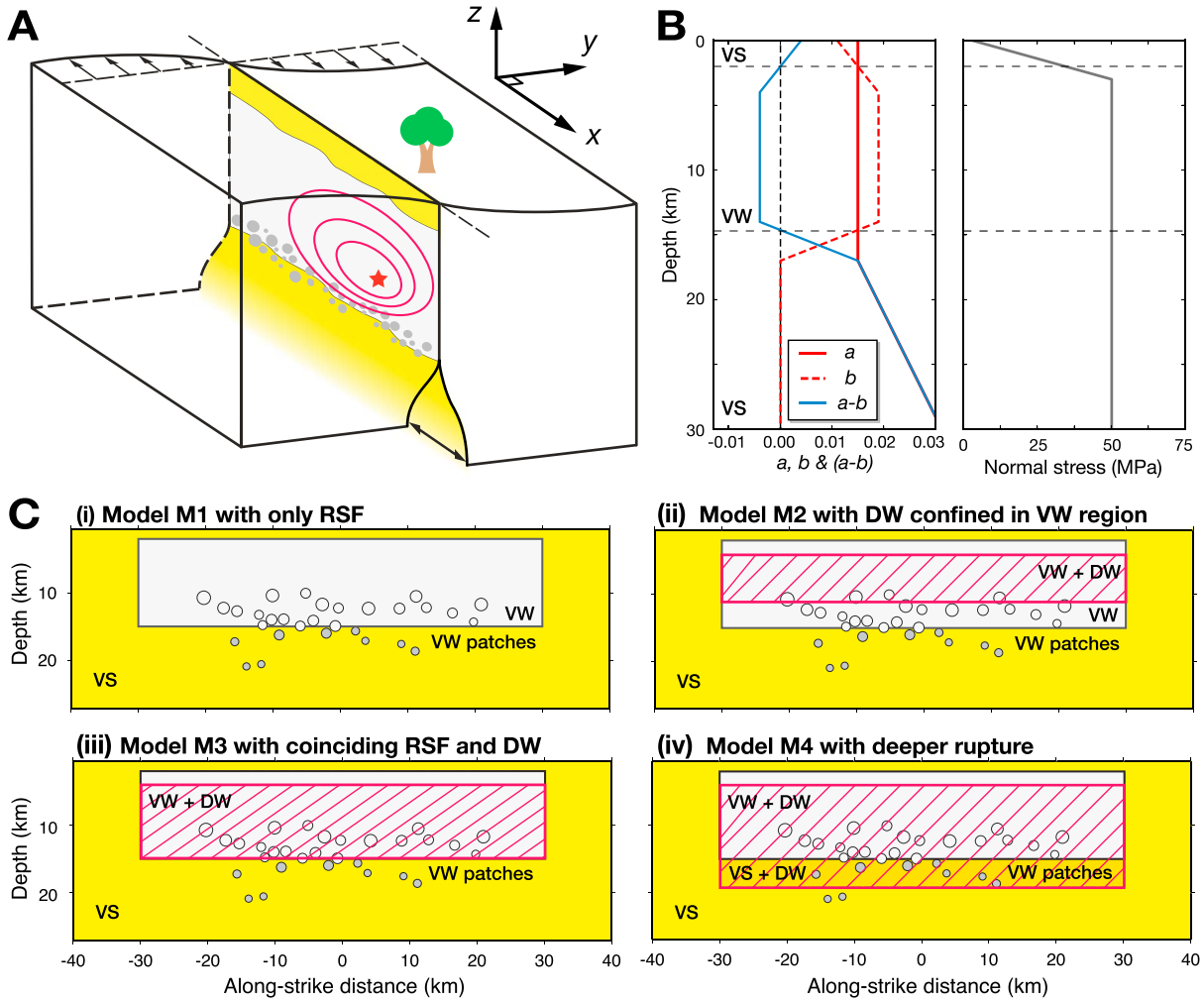

Figure 3. Our models of faults with different transitions of frictional properties with depth. (a) Schematics of the fault zone, with a 2-D planar strike-slip fault embedded into a 3-D elastic half-space. (b) Depth profiles of (left) the rate-and-state friction (RSF) parameters *a*, *b*, and *a*-*b*, and (right) the initial effective normal stress (without the effects of thermal pressurization) used in most cases. (c) (i) Model M1 with only RSF, which contains a steady-state velocity-weakening (VW) region (white) surrounded by steady-state velocity-strengthening (VS) regions (yellow). (ii) Model M2 with enhanced dynamic weakening (DW) (red hashed region) confined within the VW region. (iii) Model M3 with the depth extent of DW coinciding with the deeper VW/VS transition. (iv) Model M4 with a greater depth extent of DW than the VW/VS transition. The same set of VW patches (white circles within the VW region and gray circles within the VS region) is imposed near the VW/VS transit ion in all models to represent fault heterogeneity.

formulation for the state evolution [*Dieterich*, 1979, 1981; *Ruina*, 1983]. For each point on fault $(x, y = 0, z)$, the evolving frictional shear resistance τ obeys the following equations:

$$\tau = \bar{\sigma} f = (\sigma - p)\left(f^* + a \ln \frac{V}{V^*} + b \ln \frac{V^* \theta}{L}\right), \tag{2}$$

$$\frac{\mathrm{d}\theta}{\mathrm{d}t} = 1 - \frac{V\theta}{L}, \tag{3}$$

where the shear resistance $\tau = \sqrt{\tau_{yx}^2 + \tau_{yz}^2}$ is a product of the effective normal stress $\bar{\sigma}$ (on-fault normal compressional stress σ minus the pore pressure p) and the rate-and-state friction coefficient f. The friction coefficient f depends on two variables, slip rate $V = \sqrt{V_x^2 + V_z^2}$ and state θ, and five parameters, including the reference friction coefficient f^* at the reference slip rate V^*, the characteristic evolution distance L, and two nondimensional parameters, a and b, for the direct effect and evolution effect, respectively. All the RSF parameters are chosen as generic values from laboratory friction experiments conducted on granite at hydrothermal conditions [*Blanpied et al.*, 1995, Figure 3b], except for L (~4 mm), which is much larger than laboratory values of 1 – 100 μm but adopted here for numerical convenience, in accordance with previous studies

[*Lapusta and Liu*, 2009; *Jiang and Lapusta*, 2016]. At the steady state where $d\theta/dt = 0$, frictional stability is determined by parameter $(a - b)$: its negative values correspond to velocity weakening (VW) and unstable slip of a region larger than a critical size; its positive values correspond to velocity strengthening (VS) and stable creep of the corresponding region [*Rice and Ruina*, 1983; *Rice*, 1993; *Ben-Zion and Rice*, 1997; *Lapusta et al.*, 2000]. The critical nucleation size, h^*, can be estimated as follows for 3-D problems and $0.5 < a/b < 1$ [*Ampuero and Rubin*, 2008; *Chen and Lapusta*, 2009]:

$$h^* = \frac{\pi}{2}\frac{\mu^* Lb}{(\sigma - p)(b - a)^2}, \tag{4}$$

where $\mu^* = \mu$ for mode III and $\mu^* = \mu/(1 - \mu)$ for mode II. Our methodology uses a regularized form of equation (2) to deal with near-zero slip rates [*Lapusta et al.*, 2000; *Noda and Lapusta*, 2010].

To incorporate enhanced dynamic weakening (DW), we consider the thermal pressurization of pore fluids due to shear heating on the fault, with off-fault diffusion of fluids and heat [*Noda and Lapusta*, 2010]. The evolution of pore pressure and temperature around the fault is governed by the following equations [*Lachenbruch*, 1980]:

$$\frac{\partial T(x, y, z; t)}{\partial t} = \alpha_{\text{th}}\frac{\partial^2 T(x, y, z; t)}{\partial y^2} + \frac{\omega(x, y, z; t)}{\rho c}, \tag{5}$$

$$\frac{\partial p(x, y, z; t)}{\partial t} = \alpha_{\text{hy}}\frac{\partial^2 p(x, y, z; t)}{\partial y^2} + \Lambda\frac{\partial T(x, y, z; t)}{\partial t}, \tag{6}$$

where temperature T, pore pressure p, and shear heating source ω are functions of the location (x, y, z) and time t, α_{th} is the thermal diffusivity, α_{hy} is the hydraulic diffusivity, ρc is the specific heat capacity, and Λ is the pore pressure change per unit temperature change under undrained conditions. The shear heating source ω is due to slip and follows a Gaussian profile normal to the fault:

$$\omega = \tau V\frac{\exp(-y^2/2w^2)}{\sqrt{2\pi}w}, \tag{7}$$

where w is the effective half-width of the shear zone that accommodates slip rate V. In areas outside of DW zones, we choose sufficiently large w and α_{hy} to effectively disable DW. Although fault weakening and earthquake arrest depths likely depend on complex interactions between fault zone properties and rupture dynamics [e.g., *Platt et al.*, 2014; *Jiang and Lapusta*, 2015], we assume a fixed depth limit of fault weakening as a conceptual example and focus on its consequence on interseismic fault behavior.

The initial value of the effective normal stress in our models starts at 3 MPa at the surface, linearly increases to 50 MPa at the depth of 3 km and stays constant at that value deeper (Figure 3b). The relatively low effective normal stress over seismogenic depths compared to lithostatic overburden minus hydrostatic pore pressure is motivated by fluid overpressure advocated by several studies [*Rice*, 1992; *Sibson*, 2014; *Suppe*, 2014] and also facilitates low shear stress levels that are consistent with a "weak fault" scenario, appropriate for mature fault zones, such as the San Andreas fault [e.g., *Brune et al.*, 1969; *Lachenbruch*, 1980; *Townend and Zoback*, 2004]. The $(a - b)\bar{\sigma}$ values for the deeper part of our fault models (16–30 km) range from ~0.5 to 1.5 MPa. These values are compatible with the effective $(a - b)\bar{\sigma}$ of ~0.1–1 MPa typically inferred from postseismic studies of major continental strike-slip events, e.g., the 1992 M_w 7.3 Landers [*Perfettini and Avouac*, 2007], 1999 M_w 7.6 İzmit [*Hearn et al.*, 2002], 2002 M_w 7.9 Denali [*Johnson et al.*, 2009], and 2004 M_w 6.0 Parkfield [*Barbot et al.*, 2009; *Chang et al.*, 2013]. We also consider cases with larger $(a-b)\bar{\sigma}$ at depths and their effect on the locked-creeping transition. Note that the values of the effective normal stress discussed are relevant for interseismic times; during dynamic rupture, thermal pressurization of pore fluids lowers the effective normal stress as dictated by the coupled equations (equations (5) and (6)).

The transitions in quasi-static and dynamic friction properties can occur at different depths, since the two mechanisms are active at distinct slip-rate regimes and presumably depend on fault conditions in different ways. For example, rate-and-state friction properties are strongly influenced by temperature, pore pressure, and lithology [*Blanpied et al.*, 1995; *Scholz*, 1998; *Mitchell et al.*, 2016]. The efficiency of thermal pressurization of pore fluids depends critically on permeability and effective shear zone width [*Rice*, 2006; *Platt et al.*, 2015]. Thus, combining low- and high-slip-rate frictional properties can plausibly lead to various styles of rheological transitions.

Table 1. Parameters for Our Fault Models

Parameter	Symbol	Value		
		Fault Geometry		
Fault length	λ_x	100 km		
Fault width	λ_z	40 km		
Cell size	Δx	40 m		
Length of VW region	L^{VW}	60 km		
Depth limit of VW region	D^{VW}	15 km (M1–M4)		
Depth limit of DW region	D^{DW}	12 km (M2), 15 km (M3), 19 km (M4)		
		Elastodynamic Properties		
P wave speed	V_p	5.2 km/s		
S wave speed	V_s	3.0 km/s		
Shear modulus	μ	30 GPa		
Poisson's ratio	ν	0.25		
		Frictional Properties[a]		
		VW Region (4–14 km)	VS Region (17–30 km)	VW Patches
Rate-and-state parameters	a	0.015	0.015–0.032	0.011
	b	0.019	0.000	0.018
	L	4 mm	4 mm	3 mm
Reference friction coefficient	f^*	0.6		
Reference slip velocity	V^*	10^{-6} m/s		
		Hydrothermal Properties[b]		
Half-width of shear zone	w	10 mm		
Undrained $\Delta p/\Delta T$	Λ	0.1 MPa/K		
Hydraulic diffusivity	α_{hy}	10^{-4} m^2/s		
Thermal diffusivity	α_{th}	10^{-2} m^2/s		
		Other Conditions		
Plate loading rate	V_{pl}	32 mm/yr		
Initial effective normal stress[c]	σ_0	50 MPa		

[a]Nonuniform parameter values are linearly interpolated within each depth range and over VW/VS transitions.
[b]Hydrothermal properties are only relevant in DW regions.
[c]This is the value assigned at depths >3 km and unaffected by shear heating due to slip and thermal pressurization. The values between 0 and 3 km depth are linearly interpolated from 3 to 50 MPa.

We consider four representative scenarios, in which frictional properties of faults, including low-slip-rate RSF and/or high-slip-rate DW, follow a layered distribution (uniform along the strike and variable with depth) (Figure 3c). In the first model M1, the fault is only governed by RSF, with depth-dependent VW and VS properties based on laboratory data (Figure 3b) [*Blanpied et al.*, 1995]. Such RSF properties explain the typical depth variation in fault slip behavior [*Scholz*, 1998], lending itself to successful applications in generic models of seismogenic faults [*Tse and Rice*, 1986; *Lapusta et al.*, 2000; *Lapusta and Liu*, 2009] and models that reproduce more specific observations such as the Parkfield earthquake sequence [*Barbot et al.*, 2012]. Models M2–M4 have the same quasi-static rate-and-state friction properties as M1 and also incorporate DW with different depth limits relative to the VW/VS transition—shallower DW in M2, DW terminating at the VW/VS transition in M3, and deeper DW in M4—thereby allowing for coseismic fault weakening and large earthquake arrest at varying depths. Models M2 and M4 were previously used to illuminate the relation between the depth extent of large earthquakes and the activeness of microseismicity [*Jiang and Lapusta*, 2016]. Here we consider this expanded set of models to investigate both seismic and geodetic observables. All values for our model parameters are listed in Table 1.

In addition, we consider fault heterogeneity at transitional depths as represented by random circular patches with VW properties different from those of the main VW region, most of which are imbedded in VW fault areas with the rest surrounded by VS fault areas. These patches are designed to have an overall smaller nucleation size than the main VW region and hence greater tendency to promote microseismic events. The patch sizes are chosen to decrease with depth to indicate the eventual reduction of rheological heterogeneity with the increase of depth and temperature, which results in deepest patches being smaller than the estimated nucleation size. We only consider VW patches near the rheological transition, since patches at shallower and greater depths are expected to only participate in large events and produce isolated repeating events, respectively.

We simulate the long-term fault slip history in these models, including earthquake sequences and aseismic slip. The elastodynamic shear tractions $\tau_{yi}, i = x, z$ on the fault plane ($y = 0$) are expressed as follows [*Lapusta and Liu*, 2009]:

$$\tau_{yi}(x,z;t) = \tau_{yi}^{o}(x,z;t) + f_{yi}(x,z;t) - \frac{\mu}{2c_s}V_i(x,z;t), i = x,z\,. \tag{8}$$

In these equations, τ_{yi}^{o} are the shear tractions induced by external loading if the fault plane were constrained against any slip, f_{yi} are functional that capture wave-mediated static and dynamic stress transfers and depend on slip, slip rate, and their relevant histories, and the last term represents radiation damping [*Rice*, 1993], where μ is shear modulus and c_s is shear wave speed. The last term is separated from the rest of the response to slip and its history, contained in the functionals, to simplify their numerical calculation. Using a spectral boundary integral approach, we find the evolution of slip and shear stress on the fault by solving the elastodynamic equations of fault motion (equation (8)) coupled with the evolving frictional resistance (equations (2) and (3)) that depends, in part, on the evolving pore fluid pressure and shear zone temperature (equations (5) and (6)) through effective normal stress $\bar{\sigma} = \sigma - p$ [*Lapusta et al.*, 2000; *Lapusta and Liu*, 2009; *Noda and Lapusta*, 2010, 2013]. The free surface is approximated through a method of mirror image. With adaptive time stepping, the methodology allows us to resolve slow tectonic loading, earthquake nucleation, fully dynamic earthquake propagation, and postseismic afterslip that follows the main shock.

Accounting for full dynamic wave effects of earthquakes along with slow tectonic loading is critical for resolving the detailed evolution of individual seismic events and earthquake patterns [*Lapusta et al.*, 2000]. The differences between fault slip history in fully dynamic and quasi-dynamic models [e.g., *Hori et al.*, 2004; *Kato*, 2004; *Hillers et al.*, 2006] may be especially significant when the enhanced dynamic weakening is considered [*Thomas et al.*, 2014]. Since wave effects during earthquakes can facilitate coseismic surface rupture that is challenging to resolve [*Kaneko and Lapusta*, 2010] and we are interested mainly in the behavior at the bottom of the seismogenic zone, assuming VS properties for shallow fault areas has an additional computational advantage of reducing large slip rate variations near the surface.

To capture the evolution of shear stresses and slip rates in the model, we need to resolve two length scales: the cohesive zone size, R, important in dynamic rupture [*Palmer and Rice*, 1973; *Day et al.*, 2005] and the nucleation size, h^* (equation (4)), important during interseismic periods [*Rice and Ruina*, 1983; *Rice*, 1993; *Ben-Zion and Rice*, 1997; *Lapusta et al.*, 2000]. In our models, resolving the cohesive zone poses a more stringent criterion [*Jiang and Lapusta*, 2016]. With a cell size that is one third of the quasi-static estimate of cohesive zone size, we are able to accurately simulate seismic events in our models, including microseismicity and large earthquakes.

3. Results

3.1. Large Earthquakes and Microseismicity

The simulated long-term fault slip history in our models is characterized by stable fault creep over time scales of decades to centuries, punctuated by bursts of large earthquakes lasting tens of seconds, as well as microseismicity that occurs in the postseismic and interseismic periods (Figure 4). The spatial and temporal patterns of these phenomena differ across the models M1–M4 with varying depth transitions. In general, large fault-spanning earthquakes in the models are quasi-periodic, in the sense that they have comparable slip amplitudes and recurrence times. Note that other than the small patches to promote microseismicity, the properties of the seismogenic regions are uniform along strike, but lateral variations in coseismic slip still exist, especially in M2–M4, mostly due to interactions of complex dynamic rupture process and nonuniform stress field developed through prior slip history. There is also some variability in the recurrence intervals for the four models: 31–47, 76–183, 204–270, and 240–294 years for models M1–M4, respectively, based on more than five large events in each model. Occasionally, in M2–M3, some earthquakes rupture part of the locked

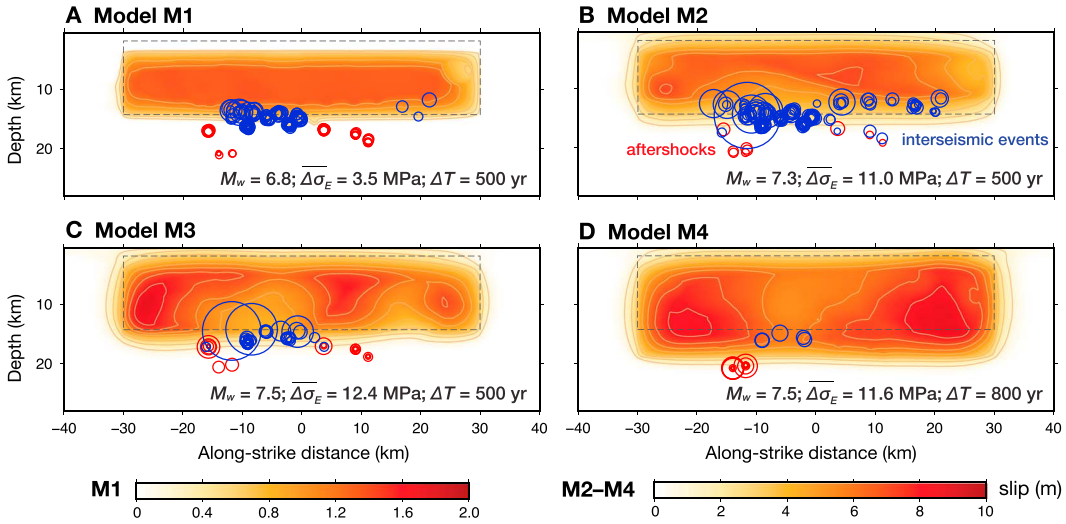

Figure 4. Spatial distribution of slip in large earthquakes and microseismicity in the fault models. Coseismic slip in typical fault-spanning large earthquakes is colored for each model, with maximum values of (a) ~1.5 m in M1 and (b–d) ~10 m for M2–M4, and contours at intervals of 0.4 m and 1 m, respectively. The moment magnitude M_w and slip-weighted average static stress drop $\overline{\Delta\sigma_E}$ for the large earthquakes are noted for all models. Microseismicity is shown for a total time window, ΔT, of 500 years for Figures 4a–4c, and 800 years for Figure 4d. The aftershocks (red circles) occur within 3 years following main shocks; the interseismic events (blue circles) occur outside the aftershock periods. Sizes of the circles are determined from a circular crack model [*Eshelby*, 1957] with equivalent seismic moments and stress drop of 3 MPa, as commonly done for natural seismicity.

seismogenic zone, creating complexities in the following interseismic period and contributing to more variable interevent times between larger events. We focus here on the more typical fault-spanning events.

Main features of these fault-spanning events, e.g., slip amplitude, recurrence interval, and average static stress drop, vary across models but are well consistent with typical observations. The maximum slip in large earthquakes is ~1.5 m in M1 and reaches ~10 m in other models, due to more prominent fault weakening aided by DW. This is reflected in different recurrence times of large events between M1 (~40 years) and other three models M2–M4 (~100–300 years). A larger depth extent of DW also leads to an increase in average fault slip during earthquakes. The smaller earthquake slip and shorter recurrence interval in model M1 resemble those of the Parkfield segment of the San Andreas fault [*Barbot et al.*, 2012]. The corresponding features of large earthquakes in models M2–M4 are largely consistent with observations from some major faults. For example, the Carrizo segment of the San Andreas fault has a recurrence interval of ~150 years for 1857-like *M*7.9 earthquakes [*Akçiz et al.*, 2010] and an average slip of ~5 to ~10 m during the 1857 event [*Sieh*, 1978; *Grant and Donnellan*, 1994; *Zielke et al.*, 2010]. Furthermore, we estimate the energy-based stress drop, $\overline{\Delta\sigma_E}$ [*Noda et al.*, 2013], to be 3.5, 11.0, 12.4, and 11.6 MPa, for the four fault-spanning events shown in Figure 4, respectively. The moment-based stress drop, $\overline{\Delta\sigma_M}$, is about 3.2, 10.0, 10.6, and 10.7 MPa for the four cases; these values are comparable to the corresponding $\overline{\Delta\sigma_E}$ and well within the seismologically estimated range of 0.3 to 50 MPa for moderate to large earthquakes around the globe [*Allmann and Shearer*, 2009].

As demonstrated in *Jiang and Lapusta* [2016], the depth extent of large earthquake ruptures, D_{rupt}, significantly influences the spatial patterns of microseismicity in the interseismic period (Figure 4). Controlled by the depth limit of VW or DW, models M1–M3 have large earthquake ruptures that are confined in the seismogenic zone, whereas M4 has deeper ruptures. Over the time periods we consider, model M2 produces the most seismicity due to complex stress and slip rate variations in the transition between the lower-stressed fully locked region (VW and DW) and higher-stressed region below (only VW). Models M2–M4 suggests that the number of small events decreases with the increase of the depth extent of large earthquakes and hence the locked region. The absence of a seismically active transition region also contributes to the delayed initiation of large events and hence larger recurrence intervals associated with M3 and M4.

3.2. The Interseismic Locked-Creeping Transition Zone

Our models reveal that interseismic fault slip rates are variable in space and evolving in time, forming a time-dependent transition zone between the shallower locked and deeper fully creeping regions.

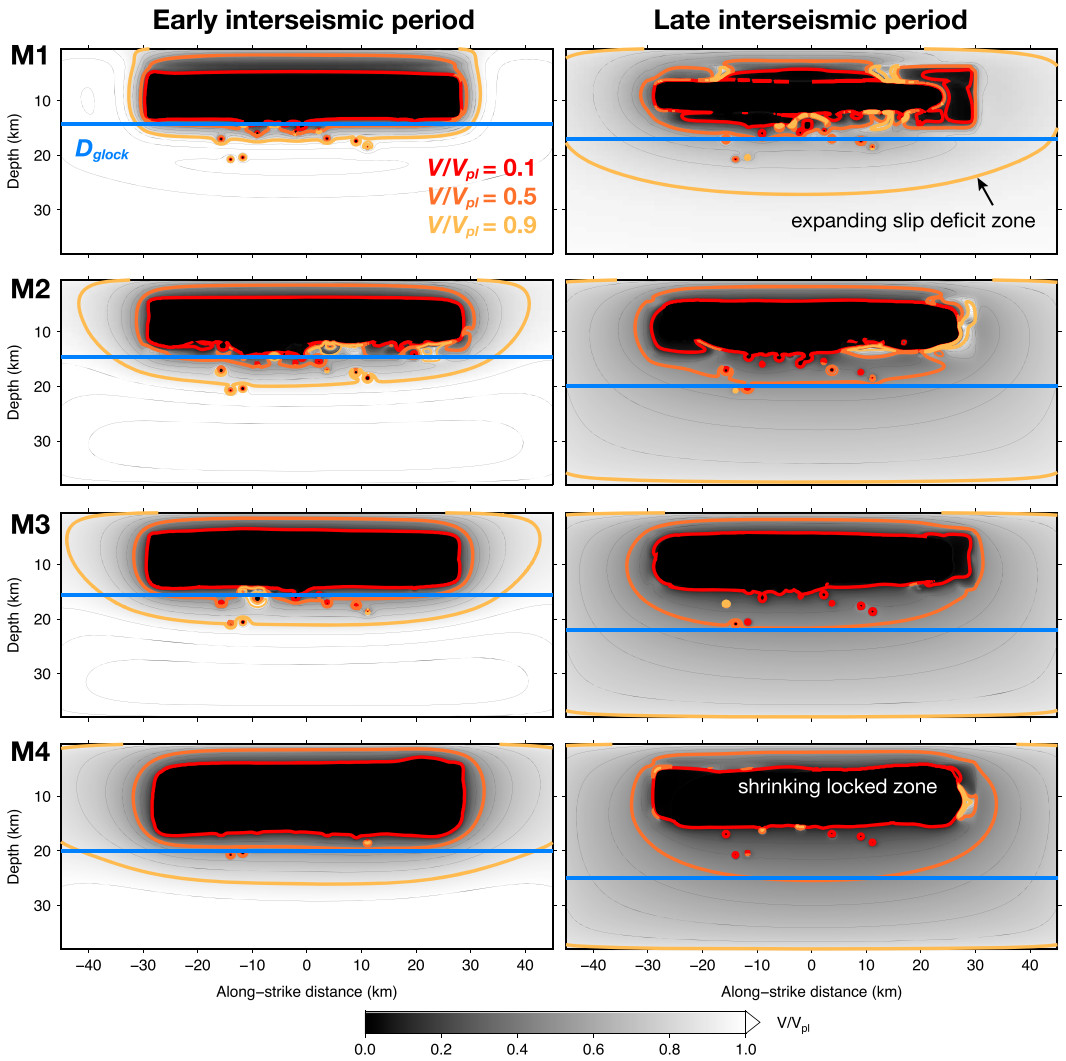

Figure 5. Time evolution of interseismic fault slip rates in the models M1–M4. Spatial distribution of slip rates on the fault, V, normalized by the far-field plate loading rate V_{pl}, is shown in gray scale colors with contour intervals of 0.1. Contours at 0.1, 0.5, and 0.9 are highlighted in red, orange, and yellow, respectively. The blue lines indicate the corresponding geodetic locking depths, D_{glock}, based on a 1-D dislocation model. (left column) The early interseismic period (1/5 of the considered recurrence intervals, which are 42, 183, 204, and 247 years for M1–M4, respectively); (right column) the late interseismic period (4/5 of the recurrence intervals).

We consider fault slip rates V, normalized by the far-field plate loading rate V_{pl} (32 mm/yr), to assess and compare the spatiotemporal evolution of interseismic creep in these models (Figure 5). Three boundaries are highlighted, where slip rates reach values of $0.1V_{pl}$, $0.5V_{pl}$, and $0.9V_{pl}$. These boundaries are of particular interest, because they indicate the approximate locations for the top, middle, and bottom of the locked-creeping transition zone.

A common feature of these models is the expansion of the locked-creeping transition zone throughout the interseismic periods (Figure 5). This transition zone, delineated by the regions with slip rates between $0.1V_{pl}$ and $0.9V_{pl}$, occurs over a broad depth range in models M2–M4 and appears more localized for model M1 in the early interseismic period. In all models, the region with slip rates lower than $0.9V_{pl}$, which we call the slip deficit region, expands in space with time. Such a process was previously attributed to the stress shadowing effect of the locked zone in the subduction zone setting [*Bürgmann et al.*, 2005; *Hetland and Simons*, 2010]. However, we note that the expansion of this region in our models is directly controlled by the amplitude and spatial extent of postseismic fault slip and to a lesser extent by the conditions of the locked zone. The evolving

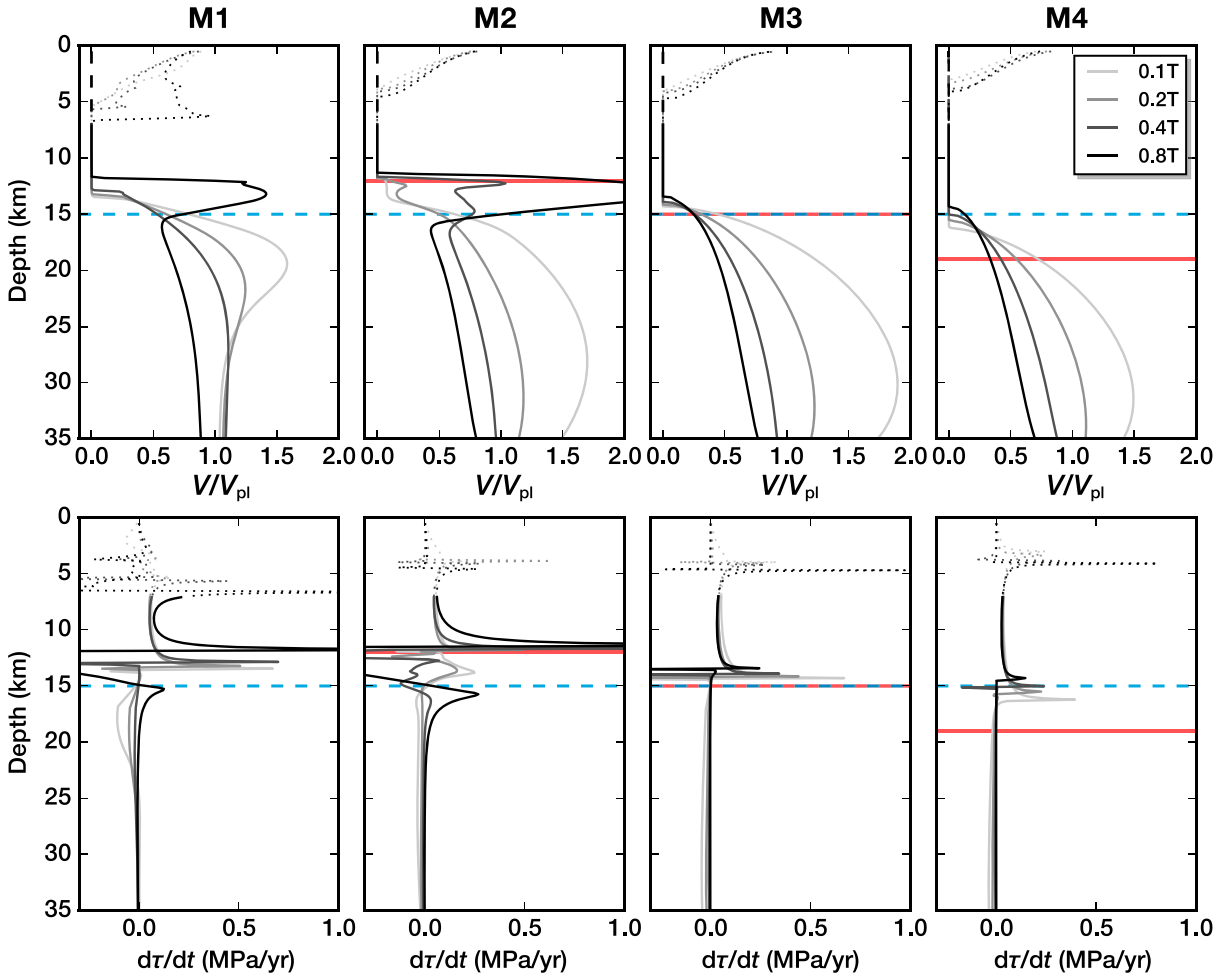

Figure 6. Time evolution of the locked-creeping transition zone and associated fault stressing rates in the models. (top row) Depth profiles of slip rates on the fault are averaged between 14 and 16 km along strike and over a 2 year time window in the interseismic periods following the large earthquake. We select four time windows centered around 0.1*T*, 0.2*T*, 0.4*T*, and 0.8*T* (*T* is the recurrence interval: 42, 183, 204, and 247 years for the considered events in M1–M4, respectively). Blue dashed lines and red solid lines mark the low-velocity VW/VS boundary and the depth limit of DW, respectively. We focus on the effects of the deeper locked-creeping transition (solid lines), and ignore slip in the shallow fault regions (dotted lines) in our surface velocity calculations, treating the shallow parts of the fault as locked (dashed lines). (bottom row) The corresponding depth profiles of the rate of the shear stress change with time. Note the clear stressing rate peaks at the upward propagating tip of the locked-creeping transition. The complex behavior of the shear stress right below the tip in models M1–M3 corresponds to the creeping in the VW region and the associated reduction of the shear stress in some regions.

slip deficit region produces time-dependent surface geodetic signals, which can be interpreted in terms of a varying geodetic locking depth, D_{glock}. We focus on D_{glock} and its time evolution in section 3.4.

The expansion of slip deficit region is also accompanied by the shrinkage of the effectively locked region (with slip rates below $0.1V_{pl}$), due to mechanical erosion from the surrounding creep until a nucleation zone of the next fault-spanning event is developed (Figure 5). Such a phenomenon is common among all our models. It is particularly prominent for M4, in which the effectively locked region reaches its maximal spatial extent immediately after the deeper coseismic rupture that involves significant parts of the VS region. In models M1–M2 and to some extent in M3, along with the eroding creep, microseismicity frequently occurs at transitional depths, thereby perturbing and obfuscating the boundary of the locked zone. We refer to the bottom edge of this locked zone—or equivalently, to the top edge of the locked-creeping transition—as the effective locking depth, D_{elock}, and study its detailed time evolution in Figure 7.

The time dependence and depth extent of the locked-creeping transition zone are more clearly depicted in the depth profiles of fault slip rates (Figure 6a). These depth profiles are each averaged between along-strike locations of $x = 14$ and 16 km (where no VW patches are located) and over a 2 year time window centered around typical times in the postseismic and interseismic period, in order to reduce the influence from nearby

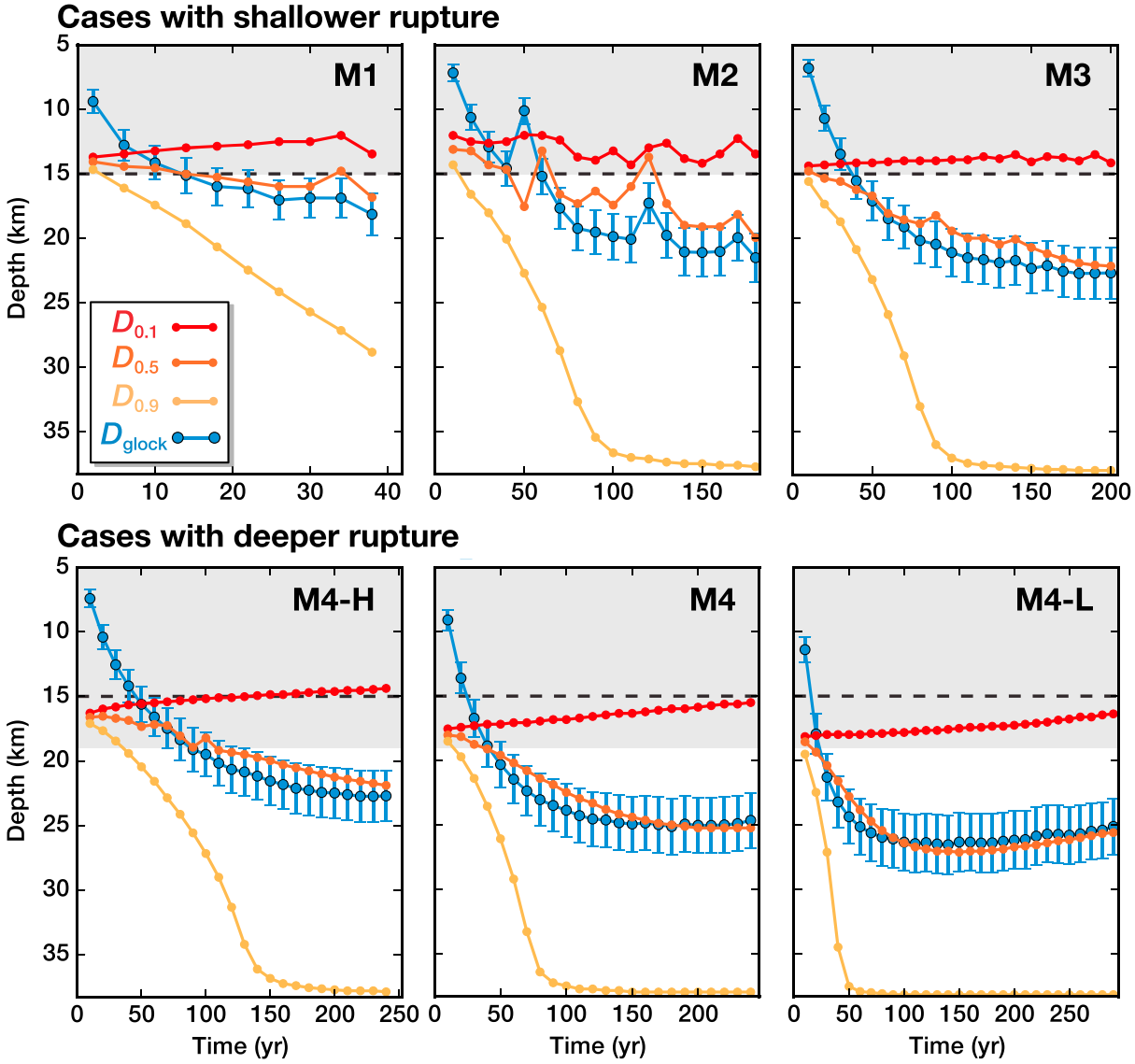

Figure 7. Time evolution of the effective and geodetic locking depths in the interseismic period of our models. Depths $D_{0.1}$, $D_{0.5}$, and $D_{0.9}$, at which fault slip rates reach certain threshold values, $0.1V_{pl}$, $0.5V_{pl}$, and $0.9V_{pl}$, are indicated in red, orange, and yellow, respectively. $D_{0.1}$ indicates the effective locking depth, D_{elock}. The inferred geodetic locking depth, D_{glock}, is shown in blue with 1σ error bars. The depth range where coseismic weakening can occur is marked in gray; the bottom of this region approximately corresponds to the depth extent of large earthquakes, D_{rupt}. The low-velocity VW/VS boundary is indicated by the dashed black line. The top three models have earthquake ruptures confined in the VW region, while the bottom three have deeper earthquake ruptures, featuring different VS properties of deeper fault extensions. The recurrence intervals are approximately 42, 183, 204, 252, 247, and 295 years.

microseismic and transient activities and to highlight the larger-scale features. In the postseismic and early interseismic period (e.g., at the time of $0.1T$ after the major earthquake, where T is the recurrence interval), most deeper fault areas experience postseismic slip with rates that are higher than the full plate rate and decay with time. In the late interseismic periods (e.g., at the time of $0.8T$), to compensate for the postseismic slip, slip rates of these fault areas drop below the full plate rate, essentially creating a locked-creeping transition zone that starts at the bottom of the effectively locked zone and extends beyond ~30 km. These transition zones deviate from a simple linear or elliptical profile and form a crack tip at the top, which induces concentrated stressing in the locked zone (Figure 6b). Where microseismicity or aseismic transients tend to occur, such as in M1 and M2, local slip rates can occasionally increase much above the full plate rate, producing an even more noncharacteristic transitional profile.

From such fault slip rate profiles, we can identify three depths below the seismogenic zone, $D_{0.1}$, $D_{0.5}$, and $D_{0.9}$, where slip rates reach $0.1V_{pl}$, $0.5V_{pl}$, and $0.9V_{pl}$, respectively, and track their detailed time evolution

in the interseismic period in M1 – M4 (Figure 7). In determining the depths, we consider a longer averaging distance along the strike than for Figure 6, between $x = 2$ and 12 km, so that the results are representative of the overall fault behavior, rather than a local section, and only mildly affected by microseismicity and partial ruptures that occur more frequently outside this range. By our definition, $D_{0.1}$ is equivalent to D_{elock}. Overall, $D_{0.1}$ (D_{elock}) either stays near the VW/VS boundary when the prior large earthquake is confined in the VW region or becomes shallower after deeper penetration of coseismic slip into the VS region. The updip migration of D_{elock} depends on the coseismic stress increase in the VS region, interseismic and long-term fault slip rates, and the product of the VS properties in deeper fault extensions and effective compressional stress [*Jiang and Lapusta*, 2016]. In contrast, $D_{0.5}$ and $D_{0.9}$ tend to deepen in all the models, as the slip deficit region (i.e., region slipping with rates lower than the plate rate) expands in the postseismic and interseismic periods. In model M2, these depth estimates are sensitive to frequent microseismicity, albeit following similar long-term increasing trends. Given that $D_{0.9}$ reaches the downdip boundary of the VS region in the late interseismic period of M2 – M4, we expect that the slip deficit region and hence locked-creeping transition zone would extend further downdip in a larger fault model with a deeper VS fault extension. On natural faults, the processes at such relative large depths of 30+ km would also depend on the distributed viscoplastic deformation in the surrounding bulk.

The time evolution of these depth estimates, as well as of the transition zone, is strongly influenced by frictional properties of the deeper fault extension; choosing more velocity-strengthening values for $(a - b)$ (or higher values of the effective normal stress $\bar{\sigma}$) would reduce the magnitude and depth extent of postseismic slip, thereby reducing the depth reach of the transition zone. This can be illustrated by comparisons between model M4 and two additional models, M4-H, and M4-L (Figure 7). The three models M4-H, M4, and M4-L have the same depth extent of DW properties that allow deeper coseismic rupture but different VS properties in terms of $(a-b)$ values; the distributions of $(a-b)$ are the same until 17 km depth (Figure 3), but follow a different slope deeper, so that the values are 0.04, 0.02, and 0.01, respectively, at the depth of 21 km. In model M4-H with higher $(a - b)$ values, the afterslip occurs with lower slip rates and it is more spatially localized, leading to a slower deepening of $D_{0.5}$ and $D_{0.9}$. In model M4-L with lower $(a-b)$ values, rapid postseismic fault slip reaches a deeper region below the locked zone and decays in amplitude quickly afterward, producing a larger slip deficit region even in the early interseismic period. However, the rapidly expanding postseismic slip does not efficiently creep updip into the locked region, which explains the slightly longer recurrence intervals (238 – 322 years) in model M4-L, compared to 240 – 294 and 212 – 280 years for models M4-H and M4. The quantitative differences between these three models further demonstrate that the slip deficit region is predominantly affected by postseismic slip in our models. The general trend of time evolution and qualitative relation between various depth estimates are similar across these three models.

Our modeling results thus suggest that the interseismic locked-creeping transition zone on fault can occur over a broad depth range, due to shrinkage of the locked zone and/or expansion of the slip deficit zone. The contribution from the shrinkage of the locked zone is most significant with deeper coseismic slip in the VS region and interseismic creep into the locked VW region. The former process can result from DW or weakly velocity-strengthening properties below the seismogenic zone, whereas the latter process depends on the nucleation size h^*. The expansion of the slip deficit zone deeper into the fault is strongly affected by how postseismic fault slip evolves in space and time. Based on steady-state friction, the postseismic fault slip rate increase $\Delta V = V/V_i$ depends on the stress elevation $\Delta\tau$ (which in turn depends on the coseismic slip distribution) and frictional parameters $(a - b)$ in the VS region: $V/V_i = \exp[\Delta\tau/(a - b)\bar{\sigma}]$, where V_i is the slip rate right before the stress change $\Delta\tau$. Consistent with our models, larger values of $\Delta\tau/(a - b)\bar{\sigma}$ at depth lead to large values of ΔV, hence rapid afterslip, and eventually a broader transition zone.

Following the considerations above, three conditions are required for the size of the locked-creeping transition to be negligible in our models: (1) limited deeper rupture due to the absence of DW and VS regions of low $(a - b)$ below the VW/VS boundary, (2) limited postseismic slip due to small $\Delta\tau/(a - b)\bar{\sigma}$ in the VS region, and (3) limited interseismic erosion in the locked zone due to small nucleation size h^*.

3.3. The Effective Locking Depth and Microseismicity

The effective locking depth $D_{\text{elock}} = D_{0.1}$ (by our definition) corresponds to higher stressing rates than the ones shallower, due to the creep in the neighboring transition zone, and hence, it could be relevant to microseismicity at transitional depths. We compare the time evolution of the depth of effective locking, D_{elock} and microseismicity between $x = -20$ and 20 km in our models in Figure 8. Note that unlike in section 3.2, we estimate D_{elock} for an even wider region, to include most microseismicity in the comparison; the resulting

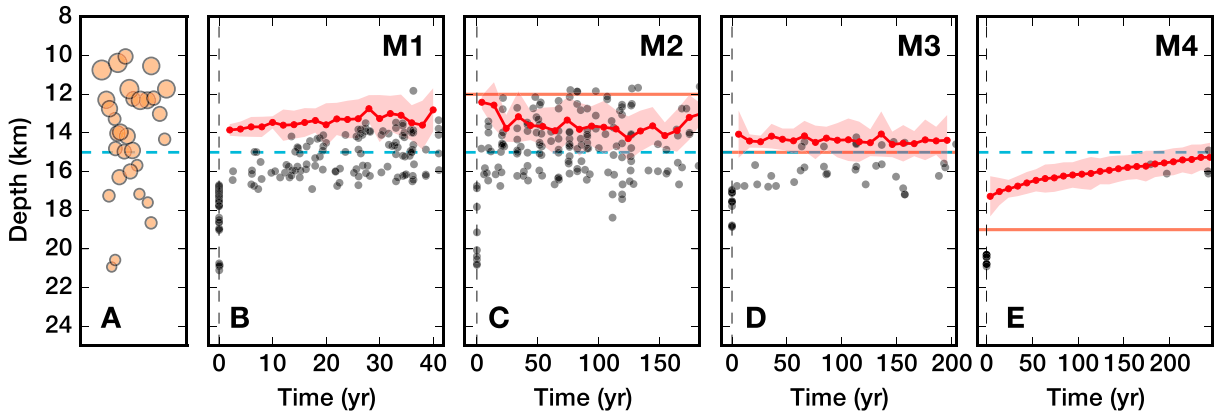

Figure 8. Time evolution of the effective locking depth, D_{elock}, and microseismicity in models M1 – M4. (a) The depth distribution of the nucleation-prone VW patches that promote microseismicity. The horizontal spacing between patches is arbitrarily scaled to focus on the depth. (b – d) The evolution of D_{elock} (red dotted lines and red colored areas) and microseismicity (grey dots) in M1 – M4. D_{elock} is estimated for the along-strike interval of x=[-20, 20] km, with red dotted lines indicating the mean values of D_{elock} and red colored areas indicating the one standard deviation range over the along-strike interval. The VW/VS boundary and depth limit of DW are denoted by the blue dashed and orange horizontal lines, respectively. Note that D_{elock} corresponds well to the upper extent of the microseismicity and its evolution.

evolution of D_{elock} is qualitatively similar but quantitatively slightly different. We illustrate the variations in D_{elock} along the fault by the shaded red area around the averaged red curve in Figure 8.

We find that indeed, in the interseismic period, the upper extent of the microseismicity approximately corresponds to the effective locking depth D_{elock} (Figure 8), even though there are nucleation-promoting patches shallower in our model. This is because D_{elock} marks the top of the locked-creeping transition zone, throughout which the fault creep rates vary and concentrated stressing arises (Figure 6). If the enhanced stressing is located within the VW fault areas, as in models M1 – M3, microseismicity is promoted, in particular, at locations of fault heterogeneity. Such considerations are supported by the strong correlation between the decreasing D_{elock} and shallower seismicity in M1 as well as the near-constant depth of both in M2 and M3. Model M4 demonstrates that when D_{elock} is deeper than the VW/VS transition, microseismicity is largely absent, occurring mostly on deeper patches positioned for generality.

When D_{elock} is above the VW/VS transition, most of the microseismicity occurs in or right next to the band between the (shallower) D_{elock} and (deeper) VW/VS transition. Hence, the microseismicity forms a prominent and relatively narrow band, the width of which approximately corresponds to the large-scale nucleation size h^*, and the depth of which corresponds to the bottom cutoff of microseismicity D_{seis}, since not many seismic events can occur spontaneously in the deeper VS fault extensions. If the band does not exist, i.e., D_{elock} is deeper than the VW/VS transition, then there is no pronounced microseismicity at the transition (M4) [*Jiang and Lapusta*, 2016].

In the postseismic periods of all four models, deeper aftershocks (i.e., between 18 and 21 km depth) appear for a limited time following large earthquake ruptures. These aftershocks occur on patches that do not produce seismicity in the interseismic period, because their sizes are chosen to be below the quasi-static estimate of the nucleation size (equation (4)). Nucleation of these aftershocks on the VW patches of subcritical sizes is made possible by the accelerated postseismic fault slip rates, indicating that the nucleation size depends on the loading rates, as was noted in earlier studies [e.g., *Kaneko and Lapusta*, 2008]. Note that such transient deep aftershocks have been observed after a number of large earthquakes [*Doser and Kanamori*, 1986; *Schaff et al.*, 2002; *Rolandone et al.*, 2004; *Jiang and Lapusta*, 2016].

3.4. The Geodetically Determined Fault Locking Depth

Here we explore how the locked-creeping transition zone is interpreted in terms of the geodetic locking depth, D_{glock}, in the traditional elastic dislocation model based on inverting surface geodetic observations [*Savage and Burford*, 1973] (Figures 9 and 10). We consider representative 1-D along-depth fault slip rate profiles derived from our models M1 and M4 (similar to Figure 6 but averaged between $x = 2$ and 12 km as for Figure 7). For three 2 year interseismic time windows in each model, we construct synthetic fault normal profiles of along-strike surface velocity based on average fault slip rates in the simulation, at stations

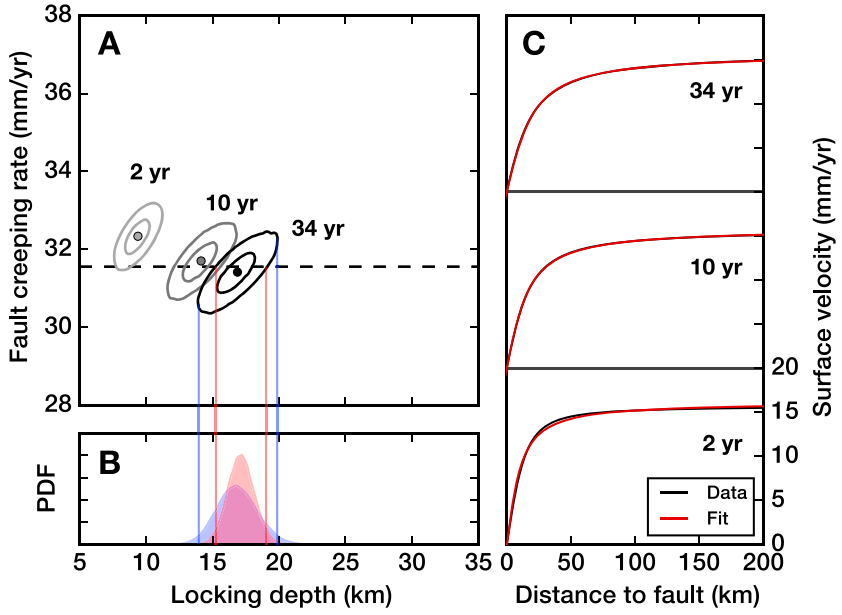

Figure 9. Estimating the geodetic locking depth and fault creeping rate in the interseismic period of model M1. (a) The joint posterior probability distribution for the geodetic locking depth, D_{glock}, and fault creeping rate, V_{cr}, is shown for three 2 year time windows in the interseismic period centered around 2, 10, and 34 years after the earthquake. Note that the recurrence interval is ~42 years. For each instance, the two parameters are inverted from the synthetic surface velocity profile based on the uniform dislocation model in a homogeneous, linear elastic half-space [*Savage and Burford*, 1973], assuming uniform and uncorrelated Gaussian observational errors of 2 mm/yr. The smaller and larger ellipses represent the 1σ and 2σ (68% and 95%) credible regions for the joint probability distribution through Gaussian kernel density estimation. The dashed line indicates the true fault creeping rate (equivalent to far-field plate loading rate) at 10^{-9} m/s (~31.6 mm/yr). (b) The marginal (blue) and conditional (red) probability density functions (PDFs) for D_{glock} correspond to an unconstrained and a perfectly constrained V_{cr}, respectively. (c) Synthetic surface velocity profiles are shown in black and their fits in red.

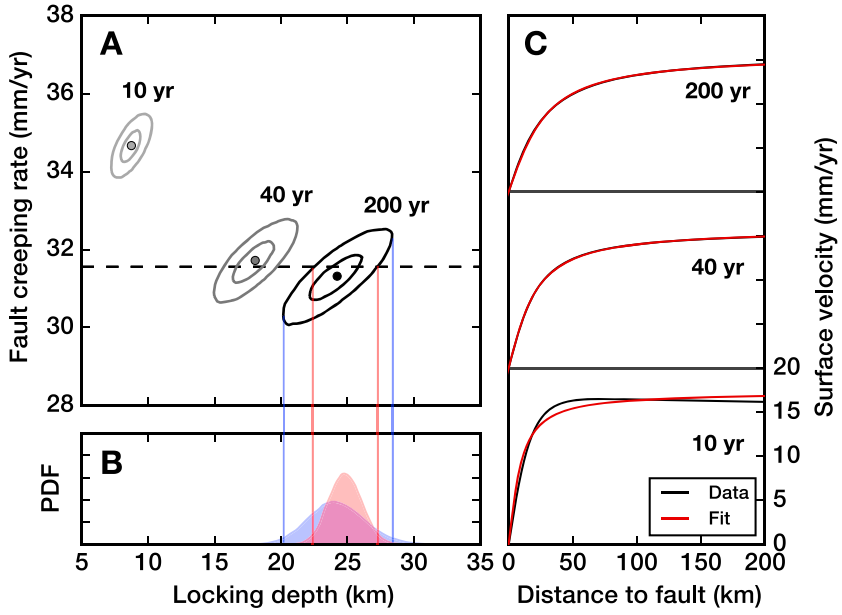

Figure 10. Estimating the geodetic locking depth and fault creeping rate in the interseismic period of model M4. Three interseismic time windows are centered around 10, 40, and 200 years. Note that the recurrence interval is ~247 years. Other plotting conventions follow Figure 9.

with a spacing of 2 km within a distance of 200 km from the fault. For the data, we assume uncorrelated Gaussian errors of 2 mm/yr, typical for modern geodetic observations [e.g., *Smith-Konter et al.*, 2011]. We then invert for D_{glock} and V_{cr} for each selected time window.

The inversion is conducted through Markov chain Monte Carlo (MCMC) sampling of the two-parameter dislocation model (PyMC package [*Patil et al.*, 2010]) in a Bayesian formulation of the inverse problem. According to the Bayes' theorem [*Bayes and Price*, 1763], the posterior distribution of model parameters is a product of the prior distribution that reflects a priori knowledge and the data likelihood function that measures the goodness of data fit. We adopt broad uniform priors for the fault creeping rate (far-field plate loading rate), $V_{\text{cr}} = \mathcal{U}(15, 50\ \text{mm/yr})$, and locking depth, $D = \mathcal{U}(5, 35\ \text{m})$, and L2 norm for the data misfit function. The joint probability density function (PDF) of D_{glock} and V_{cr} (Figures 9 and 10) indicates model parameters that generate reasonable data fit within the assumed uncertainties, with the peak of PDF representing the maximum likelihood estimate. A strong correlation exists between D_{glock} and V_{cr}, as expected from equation (1). Since we use uninformative uniform priors on D_{glock} and V_{cr}, the size of the credible regions of one and two standard deviations (1σ and 2σ) reflects the inherent uncertainty of model parameters. The marginal and conditional PDFs of D_{glock} correspond to an unconstrained and perfectly constrained V_{cr}, and thus the upper and lower bounds on the uncertainty of D_{glock}, respectively.

The inversion results for M1 and M4 suggest several common features for the estimated geodetic locking depth (Figures 9 and 10). First, surface velocity profiles in the postseismic period deviate from the form predicted by equation (1). When forced through the inversion, the data are best explained by a shallower geodetic locking depth and a higher fault creeping rate. Second, the inversions for the late interseismic periods reveal a near-constant fault creeping rate (close to the plate loading rate imposed in the model) and a geodetic locking depth that becomes deeper with time. The increase of geodetic locking depth with time is due to the decay of afterslip, which is consistent with velocity-strengthening afterslip models that are often used to explain the postseismic deformation of major earthquakes [e.g., *Johnson et al.*, 2006; *Perfettini and Avouac*, 2007; *Barbot et al.*, 2009] and kinematically similar to viscoelastic models [*Savage and Prescott*, 1978; *Meade and Hager*, 2004; *Takeuchi and Fialko*, 2013]. Third, whether the fault creeping rate is perfectly constrained or unconstrained, the geodetic locking depth is associated with large uncertainties. In particular, the uncertainties increase with the inferred geodetic locking depth, as indicated by the example of M4. Given other potential sources of uncertainties such as the heterogeneity in the Earth's structure [*Duputel et al.*, 2014], the uncertainties on D_{glock} discussed here can be regarded as ideal estimates. For natural observations, stronger prior constraints may be adopted, e.g., from geological estimates of fault slip rates [*Segall*, 2002], to maximally reduce the uncertainties and constrain the solutions.

The interseismic geodetic locking depth estimate D_{glock} lies within the locked-creeping transition zone (Figures 5 and 7). Unsurprisingly, the geodetic locking depth, based on the inversion of surface observations using an idealized model, does not exactly track the depth with certain fault slip rates as $D_{0.1}$, $D_{0.5}$, and $D_{0.9}$ do. For the postseismic period, the resultant D_{glock} lies within the actual locked zone, thus losing its intended physical meaning. Similarly, when microseismicity and aseismic transients elevate local slip rates (in M1 and M2), the resultant D_{glock} becomes shallower and less informative of the state of fault locking. In the late interseismic period, D_{glock} is close to $D_{0.5}$. We explore why this is the case in Appendix A.

3.5. Connecting Different Depth Estimates

To summarize, based on our modeling, two fault locking depths emerge relevant to seismic and geodetic observations, respectively: the effective locking depth $D_{\text{elock}} = D_{0.1}$ and the geodetic estimate of the locking depth D_{glock}. The effective locking depth D_{elock} marks the boundary above which fault areas move slowly enough to be considered fully locked ($V < 0.1V_{\text{pl}}$ by our choice) and relates to the depth of concentrated microseismicity (if it exists) and likely microseismicity cutoff D_{seis} at the bottom of the seismogenic zone. The geodetic estimate of the locking depth D_{glock} interprets surface observations by an imagined abrupt locked-creeping transition in an elastic dislocation model. D_{elock} is physically well defined, whereas D_{glock} is not always physically meaningful. Over the interseismic period, D_{elock} either stays approximately constant or becomes shallower, depending on the extent of deeper-penetrating coseismic slip (which determines how much of the deeper VS region is ruptured in an earthquake, becomes locked right after it, and gradually recovers in the interseismic period) and the large-scale nucleation size (that determines how much the creep can penetrate into the VW region). In contrast, D_{glock}, which approximately corresponds to $D_{0.5}$ at the end of the interseismic period in our models, becomes deeper throughout the interseismic period if significant

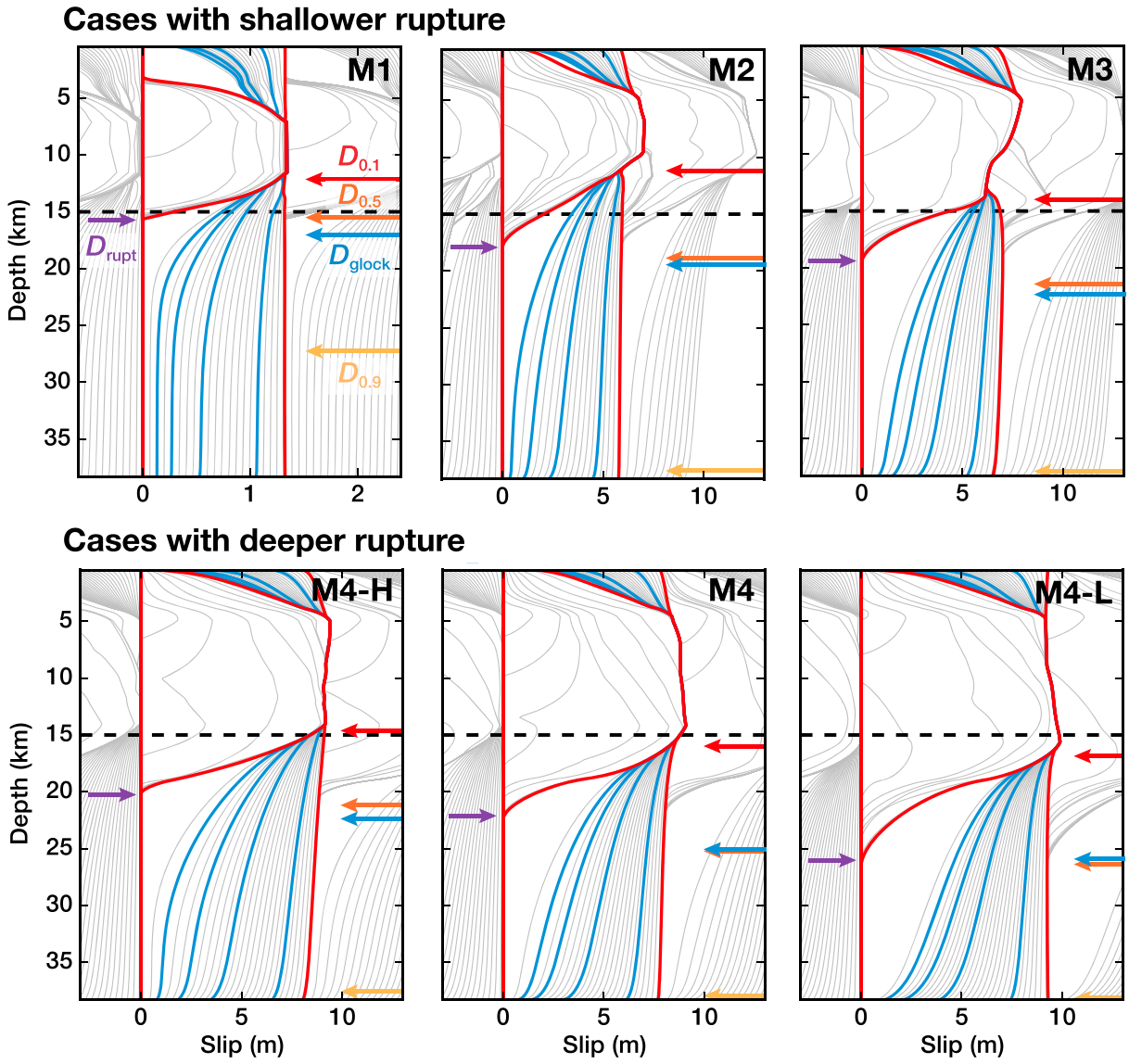

Figure 11. Cumulative fault slip along depth in our models. The slip budget during a seismic cycle is highlighted along a depth profile located at 7 km along the strike, with a coseismic period outlined by red lines and the ensuing postseismic and interseismic period indicated by five representative times in blue (0.1*T*, 0.2*T*, 0.4*T*, 0.8*T*, and *T* from left to right, where *T* is the earthquake recurrence interval). The cumulative fault slip (gray lines) is plotted for the coseismic period with intervals of 0.5 s (M1) and 1 s (the other models) and for aseismic periods with intervals of 2 years (M1) and 10 years (the other models). Depths $D_{0.1}$, $D_{0.5}$, and $D_{0.9}$ are estimated for a late interseismic period (0.8*T*) and indicated by red, orange, and yellow arrows, respectively. The geodetic locking depth, D_{glock}, estimated for a 10 year time period centered around 0.8*T*, is indicated by the blue arrow. The depth extent of large earthquake rupture, D_{rupt}, is indicated by the purple arrow. The cumulative fault slip is offset by the total slip prior to the large event. The low-velocity VW/VS boundary is marked by the black dashed line.

postseismic slip has occurred. Therefore, the two locking depths may significantly diverge toward the end of the interseismic period.

We find that the depth extent of large earthquake rupture, D_{rupt}, is shallower than the geodetically estimated locking depth D_{glock} and the closely related $D_{0.5}$ (Figure 7). Such a relation can be explained from fault slip partitioning with depth (Figure 11). Given the quasi-periodic nature of large earthquakes in our models, long-term fault slip at the plate rate is approximately balanced by the combination of coseismic, postseismic, and interseismic slip for each cycle (i.e., each large seismic event and the following postseismic and interseismic period). If, around the depth of D_{rupt} and shallower, much of the slip budget is accommodated by coseismic and postseismic slip, as it occurs in our models, then not much is left for interseismic slip, and hence D_{glock}, which represent the combined effect of the entire interseismic transition zone, tends to be deeper than D_{rupt}. In the models with deeper ruptures (i.e., ruptures penetrating below the VW/VS transition), a smaller

value of $(a-b)\bar{\sigma}$ (e.g., M4-L) facilitates a larger D_{rupt} (Figure 11); the resultant nondimensional postseismic stress change, $\Delta\tau/(a-b)\bar{\sigma}$, is also larger and leads to more significant postseismic slip and hence deeper D_{glock}. As the result, D_{rupt} is close to D_{glock} in M4-L. Larger values of $(a-b)\bar{\sigma}$ (e.g., M4 and M4-H) reduce both D_{rupt} and D_{glock} but by different amounts, with D_{rupt} shallower than D_{glock}. Overall, the depth difference between D_{glock} and D_{rupt} depend on the frictional properties at depth in a nonmonotomic way. In the extreme case with no postseismic slip, D_{rupt} would be deeper than D_{glock}, since the fault regions below D_{rupt} would have to slip with the long-term slip rate V_{pl}, and any interseismic slip penetrating up, into the seismically ruptured domain, would make D_{glock} shallower than D_{rupt}. In our scenarios with significant postseismic slip, the geodetic locking depth D_{glock} is at or below the rupture depth D_{rupt} in the late interseismic period. We have considered the case with much smaller postseismic slip (Appendix B); D_{rupt} and D_{glock} are nearly the same in that case as well.

Therefore, for a range of models, D_{glock} provides an upper bound on the depth of large earthquakes. How reliable this bound would be in practice depends on the accuracy of D_{glock}, which is subject to trade-offs with the inferred long-term fault slip rate (section 3.4) and quite sensitive to model assumptions (section 4.1).

4. Discussion

4.1. On Estimating Geodetic Locking Depth

Our modeling results suggest that a broad locked-creeping transition zone is expected for faults with deeper-penetrating coseismic slip and/or significant postseismic slip. The broad transition zone would also exist for large values of the nucleation size, a scenario that we do not focus on in this study. The geodetically estimated locking depth D_{glock} based on an elastic dislocation model is a convenient way to compare our modeling results with observations, since it is still commonly used [e.g., *Chen and Freymueller*, 2002; *Jolivet et al.*, 2009; *Lindsey and Fialko*, 2013; *Lindsey et al.*, 2013; *Materna and Bürgmann*, 2016]. The time-dependent surface deformation driven by viscoelastic processes can be equivalently mapped into time-dependent fault slip rates and locking depths in half-space models [*Savage*, 1990; *Meade and Hager*, 2004]. Even when more sophisticated methods are used for estimating the locking depth that combine the elastic dislocation model with the deeper viscoelastic substrate [*Smith-Konter et al.*, 2011], they achieve the best fit to surface data with relatively deep elastic layers, 50–100 km, suggesting that the estimated D_{glock} is dominated by the elastic dislocation model.

At the same time, the geodetically estimated locking depths for natural faults are prone to trade-offs with creeping rate estimates [*Segall*, 2002; section 3.4] and are strongly sensitive to the model assumptions. In particular, the Earth's structure around the fault is a major source of uncertainty in modeling geodetic signals. We use a heuristic example to demonstrate how ignoring elastic heterogeneity in the crust can strongly affect the inferred geodetic fault locking depth (Figure 12). In this example, we consider a broad locked-creeping transition zone (LCTZ) from M4. In a homogeneous, linear elastic half-space (Poisson's ratio of 0.25), the surface profile caused by this LCTZ results in the geodetic locking depth of ~25.5 km. Indeed, a dislocation model DSL1 with its tip at ~25.5 and the broad transition LCTZ produce nearly indistinguishable surface velocity in a homogenous, linear elastic half-space. Note that this geodetic locking depth is close to $D_{0.5}$ of the LCTZ. However, if we compute the surface profile caused by the LCTZ using a layered structure—represented by a one-dimensional reference model commonly used for Southern California [*Kanamori and Hadley*, 1975]—and then infer the geodetic locking depth using the same homogeneous half-space model, then the inferred locking depth becomes ~19.5 km, corresponding to the dislocation model DSL2 (Figure 12). However, if the bulk were a truly homogeneous elastic half-space, the locking depth would be ~25.5 km, as already discussed. The resulting discrepancy of 6 km illustrates the problem. This is because more compliant, shallow layers tend to produce more localized surface deformation that would be mapped into shallower locking depth in a homogeneous half-space. Underestimating a locking depth of about 25 km by 6 km would lead to underestimating the potency deficit on the fault by 24%.

In section 3.4, we considered the geodetically estimated locking depths D_{glock} for our models by taking a stretch of the fault close to the middle of the model, computing the average depth profile of the creeping velocities in the creeping-locked transition in the interseismic period, assigning this profile to an infinite strike-slip fault, computing the corresponding surface velocities, and using them to infer D_{glock}. Such 2-D-like analysis was done on purpose, to make our results independent of the along-strike extent

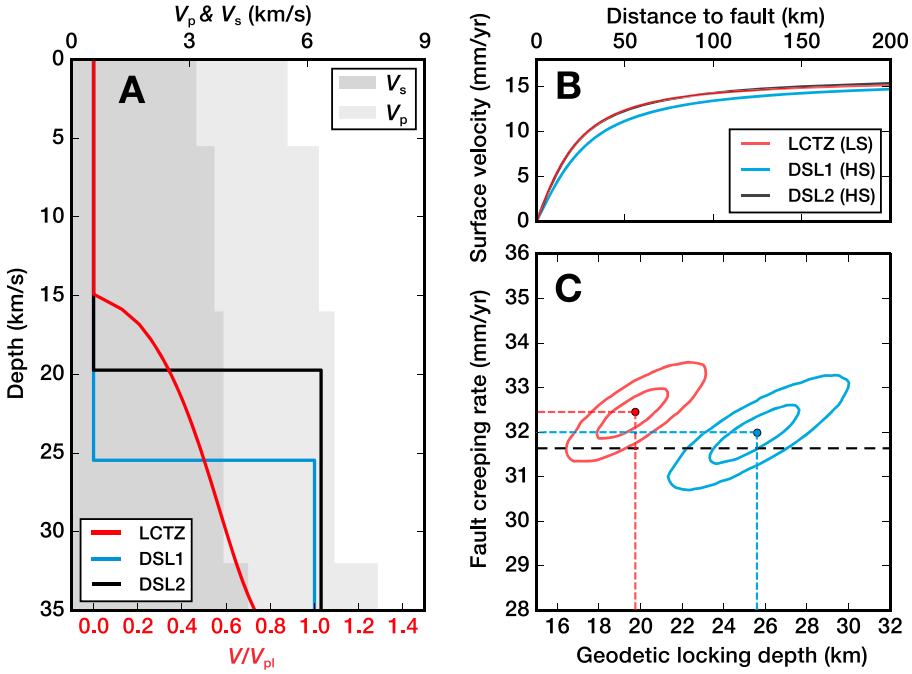

Figure 12. The effect of a layered elastic structure on estimating D_{glock} and V_{cr} in M4. (a) The locked-creeping transition zone (LCTZ, red) in model M4 and two other uniform dislocation models DSL1 (blue) and DSL2 (black). The LCTZ and DSL1 models have nearly indistinguishable surface velocity field in a homogenous, linear elastic half-space (HS). DSL2 is defined below. We consider a representative layered structure (LS) with depth-dependent V_s and V_p (dark and light gray areas) [*Kanamori and Hadley*, 1975]. (b) Fault normal profiles of along-strike surface velocity for different combinations of fault slip rate models and elastic structures. The LCTZ in the layered structure produces a surface velocity field that can be reproduced by DSL2, rather than DLS1, in a half-space. (c) Credible regions for D_{glock} and V_{cr} denoted by the ellipses, and the most plausible solutions indicated by the dashed lines. As a result, using a uniform half-space model to invert the signals produced by LCTZ in a layered structure leads to an underestimation of D_{glock}.

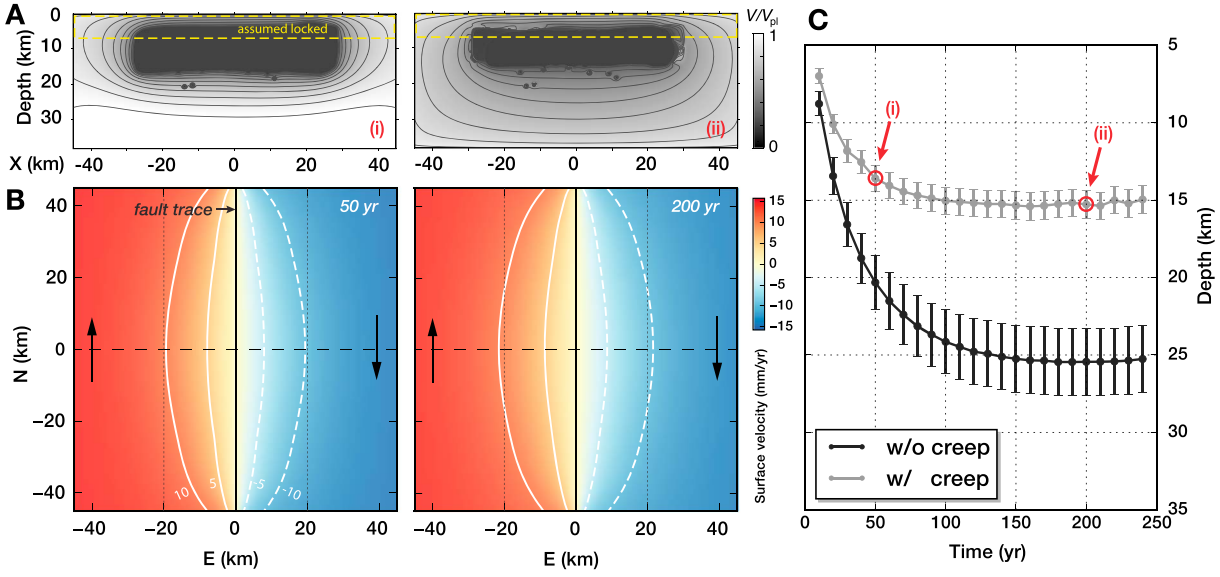

Figure 13. The effect of neighboring creeping regions on estimating D_{glock} in M4. (a) Examples of normalized slip rates on fault in the (i) early and (ii) late interseismic periods (50 years and 200 years after the earthquake, respectively; recurrence interval is 240 years) in model M4. For predictions of surface velocity, the top 7 km layer is assumed to be fully locked, to remove the influence of shallow creep and to focus on the deeper locked-creeping transition. (b) The corresponding fault-parallel surface velocity with contours in white. The surface velocity is calculated for a right-lateral fault (fault trace in black) in a 3-D homogeneous half-space problem. The velocity profile used to estimate $D_{glock\text{-}3D}$ is marked by the horizontal black dashed line. (c) Time evolution of the estimated $D_{glock\text{-}3D}$ for M4, as well as the 2-D-like estimate from Figure 7. The red circles correspond to the two times illustrated in Figure 13a and 13b.

of the VW region in our models—which is limited by numerical tractability considerations—and relevant to longer segments of the San Andreas fault. Otherwise, the VS fault creep areas that bound our simulated seismogenic zone along strike would significantly influence the overall surface velocity field and hence the estimated D_{glock}. To illustrate this point, we estimate another geodetic locking depth, $D_{glock\text{-}3D}$, and its time evolution in model M4 using our entire along-strike fault model (Figure 13a), as follows. We take the slip rate distribution over the entire fault, zero out the values for the fault areas shallower than 7 km to avoid the effects of the shallow creep and focus on the effects of the locked-creeping transition (as also done in section 3.4), and compute the surface velocities (Figure 13b). We then use the profile of surface velocities across the middle of the fault to estimate the geodetic locking depth. The resulting 3-D estimate $D_{glock\text{-}3D}$ is much shallower (~15 km in the late interseismic period), compared with the 2-D estimate (~25 km), as expected. The 3-D estimate from our models is not easy to interpret, since it is strongly affected by lateral creeping barriers placed in our model for convenience. This example indicates that it is more appropriate to compare observations from long locked fault segments with our 2-D locking depth estimates, unless pervasive fault creep is present nearby, e.g., as for the Parkfield section of the San Andreas fault which borders a creeping segment.

4.2. On Using Fully Elastic Models

In our models, the fault is embedded into an elastic half-space, while natural faults are affected by a number of inelastic processes. However, our results should provide at least a useful qualitative guidance on the interplays that are possible at the deeper fault extensions due to interaction of seismic and aseismic slip.

Compliant shallow fault zone structures have been inferred from seismic and geodetic studies for a number of faults, including Eastern California Shear Zone [*Fialko et al.*, 2002; *Cochran et al.*, 2009], northern San Andreas fault [*Chen and Freymueller*, 2002; *Jolivet et al.*, 2009; *Materna and Bürgmann*, 2016], and San Jacinto fault [*Allam and Ben-Zion*, 2012; *Lindsey et al.*, 2013]. Neglecting such features in inverting geodetic data often leads to underestimated locking depths [*Chen and Freymueller*, 2002; *Jolivet et al.*, 2009; *Lindsey et al.*, 2013]. Besides, observations of surface creep on the southern San Andreas fault [*Lindsey et al.*, 2014] indicate the possibility of distributed plastic yielding in the shallow crust, which may incur additional surface deformation and also be interpreted with shallower fault locking in simplified models. While these near-surface complexities are clearly important for properly interpreting geodetic data, they are unlikely to alter slip dynamics near the bottom of the seismogenic zone that we focus on in this work.

On the contrary, inelastic bulk relaxation (e.g., viscoelastic flow) around the deeper portions of the fault [*Bürgmann and Dresen*, 2008] and the potential switch from friction to flow within the actively shearing zone itself [*Noda and Shimamoto*, 2010; *Shimamoto and Noda*, 2014], both of which are not included in our elastodynamic friction-based models, are likely critical to capturing detailed processes near the seismic-aseismic and brittle-plastic transitions. Coupling of localized and distributed deformation has been considered in modeling postseismic geodetic signals [e.g., *Johnson et al.*, 2009; *Bruhat et al.*, 2011; *Rousset et al.*, 2012], and such approaches have only recently been extended to 2-D quasi-dynamic seismic cycle modeling [*Lambert and Barbot*, 2016]. For vertical strike-slip faults, *Takeuchi and Fialko* [2013] suggested that velocity-strengthening aseismic slip on a deep fault root and distributed deformation in a shear zone governed by rate-dependent viscoelastic rheologies are kinematically similar; they should also cause similar stressing on the fault regions updip. Hence, the overall dynamics around the transition, e.g., in terms of slip balance, stress redistribution due to slip, and the associated depth variations of slip rates, are likely to be well captured by our models, at least qualitatively.

4.3. Comparing Model Predictions With Observations

Here we compare our model predictions with available seismic and geodetic observations from major fault segments on the San Andreas fault. Our results on the divergence of the effective locking depth $D_{elock} = D_{0.1}$ related to microseismicity and the geodetically determined locking depth D_{glock} are supported by observations from several major segments of the San Andreas fault, such as the Carrizo, Mojave, and Coachella segments, which have hosted major ruptures in the past (Figure 1). For the Carrizo segment, the cutoff depths of seismicity are estimated to be 13.9, 14.4, and 16.0 km (90%, 95%, and 99%, respectively) [*Lin et al.*, 2007], which are predominantly controlled by the seismic activity near the Big Bend. The geodetic locking depth on this segment is inferred to be 18.7 ± 2 km in a 3-D viscoelastic model [*Smith-Konter et al.*, 2011]. To the south, the Mojave segment is inferred to have a geodetic locking depth of 16.8 ± 0.4 km [*Smith-Konter et al.*, 2011], whereas the seismic depth is 13–14 km [*Nazareth and Hauksson*, 2004; *Lin et al.*, 2007]. For the Coachella segment, seismicity cutoffs are at depths of 8.1, 9.3, and 14.1 km (90%, 95%, and 99%, respectively) [*Lin et al.*, 2007],

the last of which is probably sensitive to outliers. Meanwhile, geodetic studies that account for a heterogeneous elastic structure estimate a locking depth of 16.5 ± 1.8 km for a vertically dipping fault geometry [*Lindsey and Fialko*, 2013]. The shallower depths of microseismicity and deeper geodetic locking depths in these cases are consistent with the predictions of our models. The difference between the two depths may be even larger, considering that the reported geodetic locking depth may be underestimated due to reasons we discussed in sections 4.1 and 4.2. Based on our models, the difference can be explained by a combination of deeper-penetrating coseismic slip during the last major earthquake [*Jiang and Lapusta*, 2016] and deeper postseismic slip commonly observed after large earthquakes [e.g., *Marone et al.*, 1991; *Reilinger et al.*, 2000; *Hearn et al.*, 2002; *Perfettini and Avouac*, 2007]. For some other fault segments in Southern California, such as the San Bernardino, San Jacinto Valley, and San Jacinto Mountain segments, recent estimates of the geodetic locking depth are more comparable to the depth of seismicity within their uncertainties [*Smith-Konter et al.*, 2011]. The similarity of these depth estimates, if well resolved, would imply the absence of both deeper coseismic and significant postseismic slip, e.g., the behavior closer to model M1 rather than M2–M4.

Small earthquakes produced in our models reflect larger-scale fault slip processes throughout the postseismic and interseismic periods. After large earthquakes, small events occur below the ruptured zone in response to coseismic stress perturbations (Figure 4), on VW fault patches that are too small to nucleate earthquakes under slow loading rates comparable to V_{pl}. The transient occurrence of deep events in such subcritical patches implies a dependence of the nucleation size on abrupt coseismic stress changes [e.g., *Kaneko and Lapusta*, 2008] and/or on the loading slip rate, since the creeping region around the patches experiences much accelerated postseismic creep. Such behaviors of deep microseismicity in our models resemble observations of deeper aftershocks in California that followed major events such as the 1979 Imperial Valley, 1989 Loma Prieta, and 1992 Landers earthquakes [*Doser and Kanamori*, 1986; *Schaff et al.*, 2002; *Rolandone et al.*, 2004; *Jiang and Lapusta*, 2016]. Another potential explanation for such deeper events is transient brittle deformation induced by high strain rates [*Rolandone et al.*, 2004; *Ben-Zion and Lyakhovsky*, 2006]. The two explanations are physically distinct but conceptually similar, since they both point to more unstable behavior under higher stressing rates.

As the coseismically elevated stress outside of the main shock rupture area is relaxed, the interseismic evolution of microseismicity patterns reflect the state of locked-creeping transition zone. The effective locking depth, D_{elock}, at the top edge of the locked-creeping transition, is associated with concentrated stressing [*Jiang and Lapusta*, 2016]. When D_{elock} is within the VW region, concentrated microseismicity tends to occur around this depth, even in homogeneous VW regions [e.g., *Lapusta and Rice*, 2003], and especially when fault heterogeneity exists at the transitional depths, as we have postulated in our models here. Certain microseismicity patterns around seismogenic depths may indicate the state of surrounding creep, rather than the boundary of fault locking, if fault heterogeneity takes the form of isolated VW patches distributed in a larger VS region. In this case, these microearthquakes are likely to predominantly behave as repeating events [*Nadeau and Johnson*, 1998; *Chen and Lapusta*, 2009]. Detailed microseismic observations should help differentiate these scenarios in specific cases.

At least for some fault segments in California, improved seismic observations support direct connections between deeper concentrated microseismicity and the bottom of the ruptured/locked zone. For example, background seismicity and aftershocks on the Parkfield segment of the San Andreas fault forms an apparent streak that delineates the downdip edge of coseismic slip during the 2004 Parkfield earthquake [*Thurber*, 2006; *Barbot et al.*, 2012]. Similar patterns of concentrated microseismicity are found for 1984 M_w 6.2 Morgan Hill and 1989 M_w 6.9 Loma Prieta earthquakes (see summary in *Jiang and Lapusta* [2016]). In such cases, the cutoff depths of seismicity, D_{seis}, should be a reasonable proxy for D_{elock}.

Many major fault segments that have hosted great earthquakes are often seismically quiescent, such as the Carrizo and Coachella segments of the San Andreas fault (Figure 1). The extremely low levels of seismicity on those fault segments can be explained by deeper rupture extent of the prior great events, as supported by observations and numerical fault models [*Jiang and Lapusta*, 2016]. Nonetheless, there are local fault areas that are more seismically active, e.g., near the southern parts of the Cholame and Carrizo segments. The occurrence of microseismicity in those areas may be attributed to recovered creep reaching the lowermost seismogenic zone, thereby providing potential clues on the local state of fault locking.

In this study, we have used a collection of nucleation-prone VW patches as markers of fault heterogeneity and the associated microseismicity. A step beyond would be to incorporate distributions of multiscale

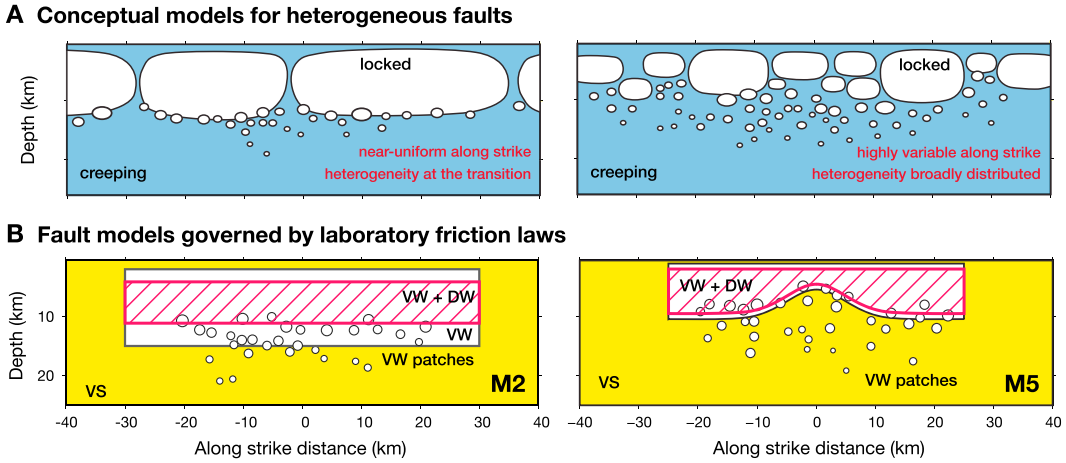

Figure 14. Models for heterogeneous faults. (a) Conceptual models. (left) Less heterogeneous faults have near-uniform properties/behavior along strike and feature relatively sharp transitions at depth with spatially concentrated heterogeneity. (right) More heterogeneous faults may be characterized by large variations of fault properties along strike and heterogeneity more randomly distributed at transitional depths. (b) Models of faults obeying laboratory-based friction laws, motivated by the conceptual models in Figure 14a. (left) Model M2, together with the other models in Figure 3, represents faults with simpler heterogeneity, and (right) model M5 represents faults with more complex heterogeneity.

heterogeneous fault properties, so that greater spatiotemporal complexity of microseismic events can be produced. Statistical properties of microseismicity can then be explored, as is often done in quasi-dynamic continuum models with heterogeneous frictional properties [e.g., *Hillers et al.*, 2006, 2007; *Dublanchet et al.*, 2013]. It remains an important future effort to study the connections between large-scale seismogenic zone behavior and statistics of microseismicity [e.g., *Hauksson*, 2010; *Tormann et al.*, 2014].

4.4. The Complicating Effect of Fault Heterogeneity

Despite the agreement between our models and available observations from several segments of the San Andreas fault, we expect that the established depth relations may be altered if rheological transitions and fault heterogeneity greatly differ from what we have considered in our models. In contrast from the other major faults in Southern California, observations from the Anza segment of the San Jacinto fault and the Imperial Valley fault [*Smith-Konter et al.*, 2011] reveal that the geodetic locking depth can be significantly shallower than the depths of microseismicity, even when a heterogeneous elastic structure is taken into account [*Lindsey and Fialko*, 2013].

The discrepancy between our models and observations from these fault segments may be attributed to significant along-strike variations in the depth dependence of fault properties (Figure 14). Faults with minor heterogeneity may have near-uniform fault properties along strike and heterogeneity, if any, concentrated at smaller scales and along the transitional depths. Such a conceptual picture motivates our models M1–M4. However, more heterogeneous faults likely feature pronounced variations in fault properties along strike and along depth. The heightened levels of heterogeneity may result from more complex geometry, lithology, pore pressure, and structure of the deeper fault zone [*Sibson*, 1984; *Mitchell et al.*, 2016]. Motivated by this concept, we consider an additional model M5 with significant along-strike heterogeneity, represented by (1) along-strike changes in the depth extent of the larger-scale VW region and (2) VW patches broadly distributed in the VS regions below the main VW region.

The long-term fault behavior in model M5 consists of frequent smaller events (M_w ~4) in the interseismic periods of occasional larger events (M_w 6–6.5) (Figure 15). In the interseismic period, fault slip rates are highly variable along strike, due to perturbations from seismic ruptures, interseismic coupling of VW patches, and the associated aseismic transients. While locally for each depth profile, at a given along-strike location, the relations between the depth of concentrated microseismicity and the extent of the locked-creeping transition suggested by our more uniform models may hold, there is no practical way to infer the local geodetically

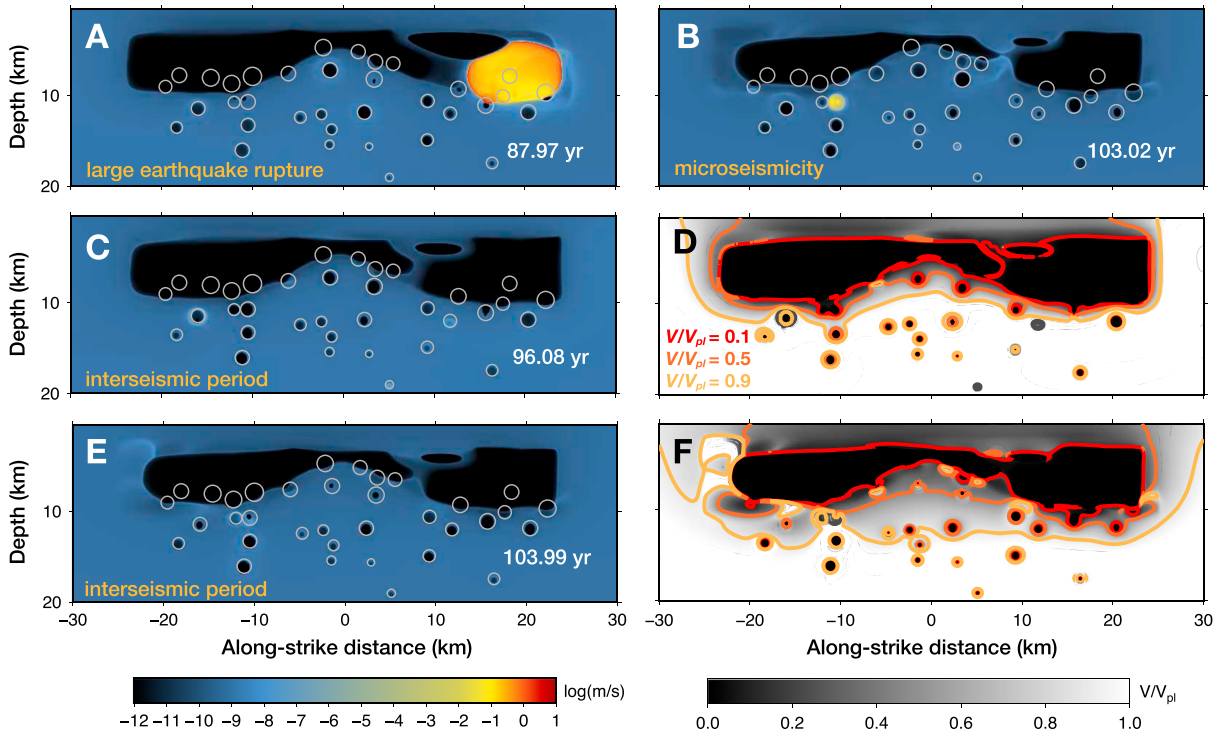

Figure 15. Complexity of fault behavior in model M5. Snapshots of (a) a large earthquake rupture, (b) a microseismic event, and (c and e) interseismic periods are shown from the long-term behavior of model M5 with logarithmic slip rates in color. (d and f) The distributions of normalized slip rates V/V_{pl} corresponding to Figures 15c and 15e are shown, respectively.

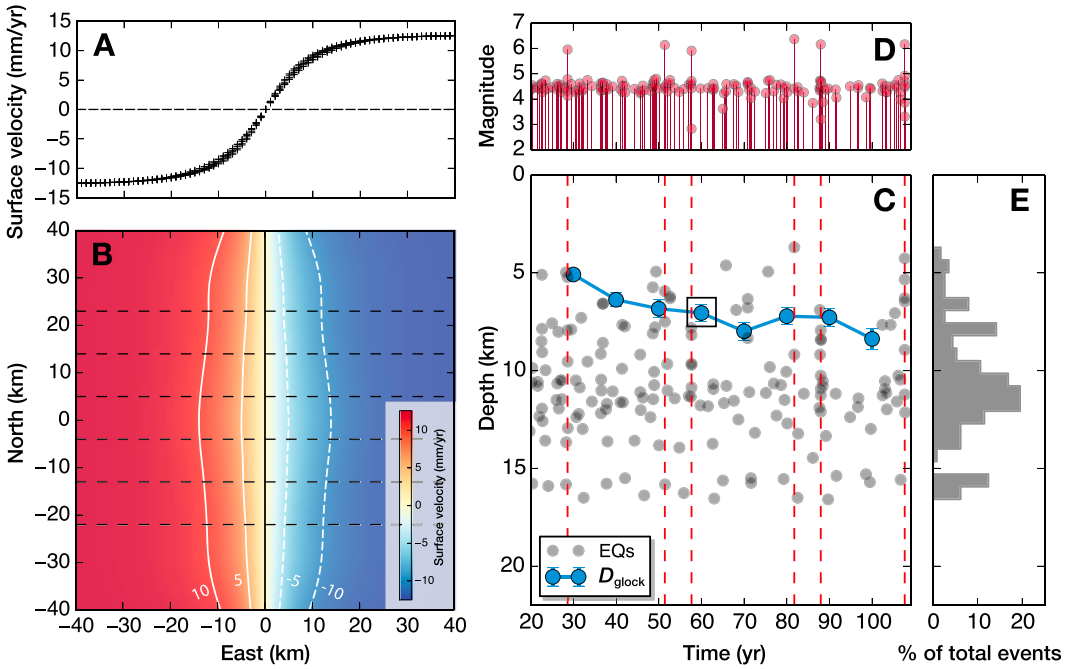

Figure 16. Shallower locking depth and deeper seismicity in model M5. (a) Stacked profiles of the north components of the surface velocity that are used to invert for the D_{glock} of the segment. (b) The 2-D surface velocity field in the interseismic period of model M5 with contours at intervals of 5 mm/yr. Locations of the velocity profiles are shown as the black dashed lines. The fault is assumed fully locked at depths shallower than 5 km with its surface trace represented by the black vertical line. (c–e) Time evolution of the apparent geodetic locking depth for this segment and the depth of seismicity (Figure 16c), with the magnitudes and overall depth distribution of seismicity shown in Figures 16d and 16e, respectively. D_{seis} is deeper than D_{glock} in this model with significant along-strike variations and more seismogenic patches in the VS areas. The time period considered in Figures 16a and 16b is indicated by the black square in (c).

determined locking depth from surface observations, given its rapid variations along strike and all the trade-offs discussed earlier. Hence, instead, let us consider the 3-D-like estimate $D_{\text{glock-3D}}$ of the interseismic geodetically determined locking depth (section 4.1) obtained for the entire segment (Figure 16). To obtain the estimate, we stack the dashed profiles from Figure 16b. Note that the estimate is affected by the creeping regions on the sides of the main VS region, as demonstrated in section 4.1. The resulting $D_{\text{glock-3D}}$ stays with time at the depths of 6–8 km, while much of the microseismicity occurs below. The estimated shallower depth of geodetic locking is due to both the heterogeneous—and shallower on average—VW/VS boundary as well as the creeping regions on the sides of the main VS region. The deeper microseismicity in this model reflects the chosen broad distribution of the VW patches within the creeping region in conjunction with the spatial and temporal evolution of fault creep. Many of these deeper events are repeating sequences. This model demonstrates that significant fault heterogeneity can alter the relation between microseismicity and geodetic fault locking depth.

As an example of tailoring fault models to specific fault segments, *Jiang and Fialko* [2016] postulated that a broad transition zone with stochastic heterogeneity in frictional properties exists at the bottom of the seismogenic zone on the Anza segment of the San Jacinto fault. They argued that such a form of fault heterogeneity is more plausible than a more organized structure considered in model M5, since repeating earthquakes are not commonly observed in the Anza region. Their models successfully produced microseismicity, with spatiotemporal complexities, much below the geodetic locking depth on the Anza section, indicating that a more complex transition of fault friction with depth should be considered for some fault segments.

Note that even on segments with such pronounced VW/VS heterogeneity, a large coseismic rupture penetrating much below the VW/VS transition—and all of its assumed complexity—may still lead to postevent behaviors like in model M4, at least for a while. However, such deeper penetration over the entire segment would imply more uniform dynamic (high slip rate) weakening properties than rate-and-state (low slip rate) ones.

4.5. Relevance for Thrust Faulting

We have developed our models with a focus on strike-slip faults, but the basic ideas and results from our modeling should also be applicable to faults at other types of plate boundaries, such as subduction zone megathrusts. The shallow-dipping thrust faults may allow for an even broader transition zone than near-vertical strike-slip faults, which enables distinct fault slip behavior at transitional regimes [*Schwartz and Rokosky*, 2007; *Lay et al.*, 2012]. Better depth resolution provided by the location of GPS stations with respect to different depths of the megathrusts in many regions facilitates the popular use of spatially variable fault coupling rather than a single geodetic locking depth [e.g., *Kaneko et al.*, 2010; *Ader et al.*, 2012]. As long as the layered distribution of frictional properties considered in M1–M4 is qualitatively applicable, one would expect qualitatively similar spatial relations between fault interface seismicity, locked-creeping transition, and slip deficit zone (Figures 4 and 5).

Observations from the Himalayan and northeastern Japan subduction zones provide supporting examples for the ideas of expanding slip deficit zone (corresponding to deepening of $D_{0.5}$ and $D_{0.9}$) and shrinking locked zone (corresponding to shallowing of $D_{0.1}$), as observed in our models M1–M4. On the Main Himalayan Thrust in Nepal, background microseismicity is concentrated at the downdip edge of coseismic slip during the 2015 M_w 7.8 Ghorka earthquake [*Avouac et al.*, 2015; *Yue et al.*, 2016], whereas the geodetically inferred slip deficit zone extends further downdip in the interseismic period preceding the event [*Ader et al.*, 2012; *Stevens and Avouac*, 2015]. The spatial relation between downdip limits of coseismic rupture and interseismic coupling resembles our modeling results. In northeastern Japan where the 2011 M_w 9.0 Tohoku-oki earthquake struck [*Simons et al.*, 2011], analyses of onshore GPS measurements and repeating earthquakes indicate that fault areas downdip of the main shock rupture experienced accelerating slip or updip migration of deep aseismic slip over 15 years prior to the event [*Mavrommatis et al.*, 2014, 2015]. After the Tohoku-oki earthquake, these creeping fault areas apparently became locked, as repeating earthquakes within the region became inactive, implying that the spatial extent of the coseismic rupture was larger than the interseismically locked zone and included areas that had been creeping before the event [*Uchida and Matsuzawa*, 2013].

Some megathrust faults feature more complex styles of slip in the transition zone. For instance, Cascadia subduction zone is seismically quiescent and hosts frequent slow slip transients downdip of the seismogenic zone [*Dragert et al.*, 2001]. Such transients can result, in a limited parameter range, on faults with standard

rate-and-state friction [*Liu and Rice*, 2005, 2007; *Perfettini and Ampuero*, 2008], and we see such transients in our models, on the scale of the nucleation size. To have more pronounced transients in our models, we need to incorporate broad VW transition regions with large nucleation sizes. The aseismic transients can be more robustly reproduced in models with more complex frictional properties and the associated pore fluid conditions, such as pore pressure effects due to inelastic dilatancy [*Liu and Rubin*, 2010; *Segall et al.*, 2010] and $(a-b)$ values that depend on slip rate [*Shibazaki and Iio*, 2003]. Considering the relation between interseismic slip that includes such transients, the depth extent of the coseismic rupture, and microseismicity is an important topic for future work.

5. Conclusion

We have developed models of faults with different depth-dependent frictional properties around the bottom of the seismogenic zone, to explore the relation between the depths of microseismicity, interseismic fault locking, and large earthquakes. Our models incorporate laboratory-based rate-and-state friction laws and enhanced dynamic weakening mechanisms in a layered distribution of fault properties. Using a comprehensive set of models, we find that the locked-creeping transition zone occurs over a broad depth range in cases with coseismic slip penetrating into the deeper creeping (VS) fault extensions and/or deep and pronounced afterslip. The effective locking depth (D_{elock}) near the top of the locked-creeping transition either stays nearly constant (if there is no coseismic slip in the deeper creeping fault extensions) or becomes shallower with time (if there is such deeper coseismic slip). When located within the VW region, D_{elock} promotes microseismicity due to its concentrated loading, and it is closely associated with the cutoff of microseismicity, D_{seis}, in our models. The deeper portions of the locked-creeping transition, associated with creep at 50–90% of the long-term rate, tend to deepen after the postseismic period, compensating for any deeper coseismic slip and/or afterslip. Hence, the locked-creeping transition broadens toward the end of the interseismic period. The geodetic locking depth (D_{glock}), estimated from interseismic surface velocities using the traditional 2-D elastic dislocation model, approximately corresponds to the depths of creep at about 50–60% of the long-term rate in the middle to late interseismic period and hence also deepens with time.

Our model predictions are consistent with the available seismic and geodetic observations for the Carrizo, Mojave, and Coachella segments on the San Andreas fault, where the depth cutoff of microseismicity is shallower than the geodetically estimated locking depth. Our modeling results suggest that this difference between the seismic and geodetic estimates of the seismogenic zone can be quite significant and reflects the broad—and potentially broadening with time—extent of the locked-creeping transition for these segments. The difference may be even more significant than currently estimated, considering potential underestimation of D_{glock} due to simplified structure assumptions, inelastic yielding near the surface, and/or 3-D effects. Based on our models, the observed differences between D_{seis} and D_{geod} suggest that these fault segments experienced a combination of deeper coseismic slip and extensive afterslip in prior large earthquakes. The absence of concentrated microseismicity at the bottom of the seismogenic zone on these segments further supports the possibility of deeper coseismic slip [*Jiang and Lapusta*, 2016]. In principle, a well-resolved difference between D_{elock} and D_{glock} can be used to constrain, through numerical modeling, the extent of deeper-penetrating coseismic slip and the amplitude and spatial extent of postseismic slip in preceding large events.

On such fault segments, assuming that the cutoff depth of microseismicity coincides with the geodetic locking depth D_{glock} would lead to underestimated long-term creeping rates V_{cr}. This is because the assumption would result in D_{glock} shallower than the actual one, and the surface observations would then be best matched with a creep rate lower than the actual one (e.g., section 3.4). Hence, the underestimation of D_{glock} may be among the reasons that cause the apparent discrepancy between the geodetic and geological estimates of slip rates on some fault segments [e.g., *Chuang and Johnson*, 2011; *Tong et al.*, 2014].

Significant fault heterogeneity can complicate the relation between the different depth estimates. Discrepancies between observations and our model predictions may point to more heterogeneous fault properties than envisioned in this work [e.g., *Jiang and Fialko*, 2016]. The integration of refined geodetic and seismic observations with models of dynamic earthquakes and fault creep would provide an important avenue to probe the rheological properties of fault zone at depth and to assess the seismogenic behavior of faults and associated seismic hazard.

Appendix A: Geodetic Estimates of the Locking Depth and Moment Deficit Accumulation

In a 2-D antiplane problem, the interseismic surface velocity profile is directly related to the total moment deficit accumulation rate on the fault [*Tong et al.*, 2015]. If a simplified model, e.g., a uniform dislocation model, can produce near-identical surface velocities to our fault models with a more complex locked-creeping transition zone, then we can determine the parameters of this simplified model based on the moment deficit accumulation, without going through an inversion of the surface velocity field.

The moment deficit accumulation rate per unit length, m, depends on the depth distribution of slip deficit rate $s(z)$:

$$m = \mu \int_{-\infty}^{0} s(z)\mathrm{d}z\,. \tag{A1}$$

In a 2-D antiplane problem with a homogeneous, linear elastic half-space, the fault-parallel surface velocity $v(x)$ due to interseismic slip rates on the fault $s(z)$ is expressed as follows [*Segall*, 2010]:

$$v(x) = \frac{1}{\pi}\int_{-\infty}^{0} s(z)\frac{x}{x^2+z^2}\mathrm{d}z. \tag{A2}$$

To connect surface velocities to the moment deficit accumulation rate, consider a quantity, q, based on only the surface velocity, as the integral of velocity $v(x)$ times the distance to the fault x [*Tong et al.*, 2015]:

$$q = \lim_{W\to\infty}\left[\frac{1}{W}\int_{-W}^{W} x\,v(x)\mathrm{d}x\right], \tag{A3}$$

where W is the distance to the fault in the fault normal direction. The normalization factor, $1/W$, ensures a finite q as W approaches infinity. Inserting equation (A2) into equation (A3), one finds that q is proportional to the moment deficit accumulation rate m:

$$\begin{aligned} q &= \frac{1}{\pi}\int_{-\infty}^{0} s(z)\lim_{W\to\infty}\left[\frac{1}{W}\int_{-W}^{W}\frac{x^2}{x^2+z^2}\mathrm{d}x\right]\mathrm{d}z \\ &= \frac{2}{\pi}\int_{-\infty}^{0} s(z)\lim_{W\to\infty}\left[1-\frac{z}{W}\arctan\left(\frac{W}{z}\right)\right]\mathrm{d}z \\ &= \frac{2}{\pi}\int_{-\infty}^{0} s(z)\mathrm{d}z = \frac{2m}{\pi\mu} \end{aligned} \tag{A4}$$

The equivalent forms for q in equations (A3) and (A4) indicate that if the surface velocity $v(x)$ are nearly identical between different models, the associated moment deficit accumulation rate on the fault must also be nearly the same. The moment constraint can thus be used to find an equivalent uniform dislocation model that can produce a surface velocity field similar to that in our models M1 – M4, at least for the late interseismic periods when the velocity profile is simpler. Such theoretical considerations also allow for estimating interseismic moment deficit accumulation on faults, such as the central and southern San Andreas faults, directly from geodetic measurements of surface velocity field, without the need to invert for the fault locking depth D_{glock} and creeping rate V_{cr} [*Tong et al.*, 2015].

Focusing on the moment, rather than inversions of surface observations, facilitates the comparison of the locked-creeping transition zone in our models and other analytic solutions. We consider fault slip rate profiles based on three classic models [*Segall*, 2010] : (1) a uniform dislocation $V_{\mathrm{ud}}(z)$, (2) a modified constant stress drop crack $V_{\mathrm{cc}}(z)$, and (3) a modified tapered crack $V_{\mathrm{tc}}(z)$, characterized by the following closed-form expressions:

$$V_{\mathrm{ud}}(z) = \begin{cases} V_{\mathrm{pl}} & z \geqslant D_{\mathrm{ud}}\,, \\ 0 & z < D_{\mathrm{ud}}\,, \end{cases} \tag{A5}$$

$$V_{\mathrm{cc}}(z) = V_{\mathrm{pl}}\sqrt{1-\left(\frac{D_{\mathrm{pl}}-z}{D_{\mathrm{pl}}-D_{\mathrm{cc}}}\right)^2}, \quad D_{\mathrm{cc}} \leqslant z \leqslant D_{\mathrm{pl}}, \tag{A6}$$

$$V_{\mathrm{tc}}(z) = V_{\mathrm{pl}}\left[1-\left(\frac{D_{\mathrm{pl}}-z}{D_{\mathrm{pl}}-D_{\mathrm{tc}}}\right)^2\right]^{\frac{3}{2}}, D_{\mathrm{tc}} \leqslant z \leqslant D_{\mathrm{pl}}, \tag{A7}$$

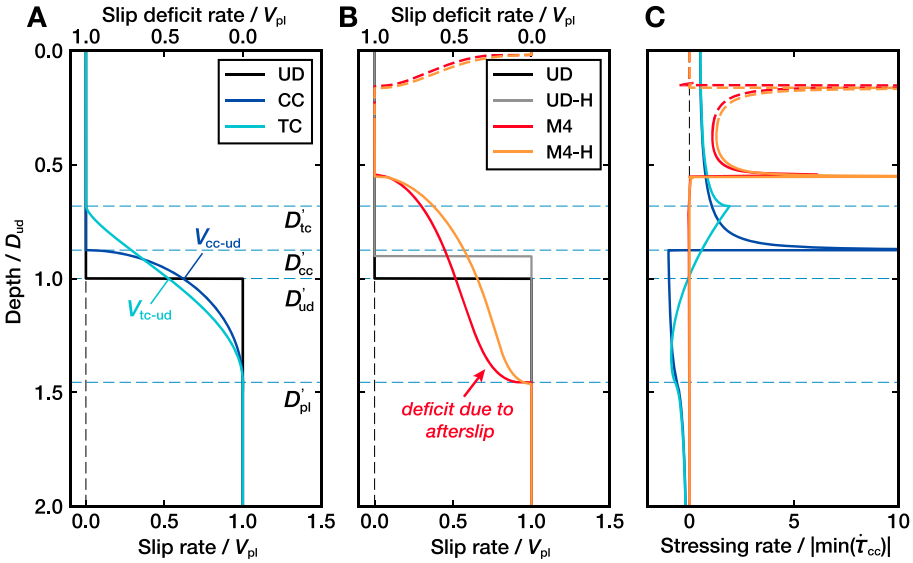

Figure A1. The distribution of (a–b) slip rates and (c) stressing rates with depth illustrating the locked-creeping transition zone in the simplified analytical models (UD: uniform dislocation; CC: constant stress drop crack; TC: tapered crack) and models M4 (red line) and M4-H (yellow line). The depth, slip rate, and stressing rate are normalized by D_{ud}, V_{pl}, and $|\min(\dot{\tau}_{cc})|$ (amplitude of the minimum stressing rate of the CC model), respectively. D'_{ud}, D'_{cc}, D'_{tc}, and D'_{pl} refer to normalized depths. UD, CC, and TC have the same moment deficit accumulation rate as M4 (by design), and UD-H has the same moment deficit accumulation rate as M4-H. The shallow portion of the profile in M4 and M4-H (red and orange dashed lines, respectively) contributes to the stressing in the locked zone, but it is not our focus. The horizontal dashed lines indicate some of the boundaries of the transition zone in different models.

where D_{ud} is the depth of dislocation tip, D_{cc} and D_{tc} correspond to the depth of the crack tips in the two crack models, and D_{pl} is the depth at which fault slips at full creeping rate V_{pl}. For modified crack models, $V_{cc}(z)$ and $V_{tc}(z)$ are equal to 0 for $z < D_{cc}$and $z < D_{tc}$, respectively, and equal to V_{pl} for $z > D_{pl}$. The corresponding slip deficit rate functions can be calculated through $s_{ud}(z) = V_{pl} - V_{ud}(z)$ and similarly for $s_{cc}(z)$ and $s_{tc}(z)$. To consider a nondimensional problem, we normalize the slip rate by V_{pl} and the depth by D_{ud}.

The three models can produce similar surface velocity profiles [e.g., *Segall*, 2010, *Lindsey and Fialko*, 2013]. Assuming the same moment deficit accumulation rate, we can solve for the relation between model parameters D_{ud}, D_{cc}, D_{tc}, and D_{pl}:

$$D_{cc} = D_{pl} - \frac{4}{\pi}(D_{pl} - D_{ud}), \quad D_{tc} = D_{pl} - \frac{16}{3\pi}(D_{pl} - D_{ud}), \tag{A8}$$

In order to directly compare our model M4 with these simplified models, we choose $D_{pl}/D_{ud} = 1.45$ based on an interseismic fault slip rate profile in M4 (corresponding to 0.8T in Figure 6).

These models, with the same moment deficit accumulation rates and hence surface velocities, are shown in Figure A1. Although they are almost indistinguishable from surface observations, they have considerably different fault stressing rates with depth (Figure A1b). Near the top of the transition zone, the shape of the transition in model M4 is similar to the constant stress drop crack model, with the rapid decrease of slip rates and increase of stressing toward the shallower locked region. At greater depths near the fully creeping regions, M4 deviates from both models, with a significant slip deficit associated with the prior afterslip. If postseismic slip were much smaller, we would expect a closer match between M4 and the constant stress drop crack model.

While the location of the crack tips, D_{cc} and D_{tc}, depend on the bottom of the transition zone, D_{pl}, the slip rates at the depth of the tip of the equivalent uniform dislocation model, denoted as $V_{cc\text{-}ud}$ and $V_{tc\text{-}ud}$, are independent of D_{pl} and, in fact, correspond to a certain fraction of the long-term creeping rate V_{pl}. The two slip rates can be obtained by inserting equation (A8) into equations (A6)–(A7) and setting $z = D_{ud}$:

$$V_{cc\text{-}ud} = \left(1 - \frac{\pi^2}{16}\right)^{\frac{1}{2}} V_{pl} \approx 0.62 V_{pl}, \quad V_{tc\text{-}ud} = \left(1 - \frac{9\pi^2}{256}\right)^{\frac{3}{2}} V_{pl} \approx 0.53 V_{pl}, \tag{A9}$$

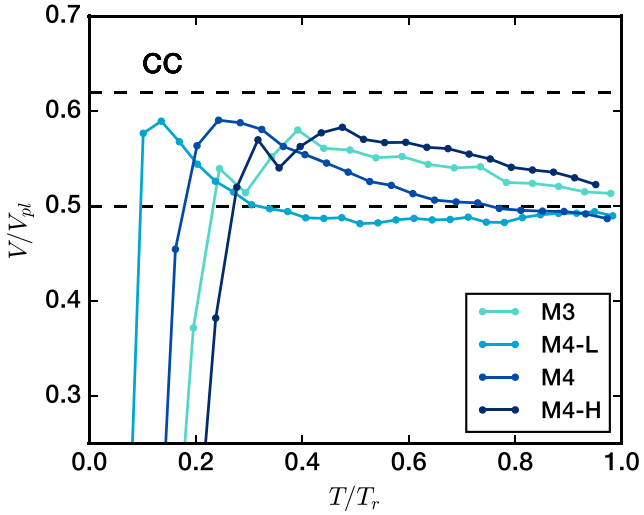

Figure A2. Fault slip rates at the depth of D_{glock} in models M3, M4-L, M4, and M4-H. The slip rates and time are normalized by the plate loading rate and respective recurrence intervals. The expected nondimensional slip rate value of 0.62 for a modified constant stress drop crack (CC) model and the value of 0.5 expected for a transition zone that is symmetric around its midpoint are indicated by dashed lines.

Furthermore, for a slip rate distribution symmetric about the point of $0.5V_{pl}$, the depth of the equivalent uniform dislocation model will coincide with the depth creeping at $0.5V_{pl}$, as follows from the moment deficit accumulation rate equivalence for the two models.

Overall, for the transition distributions considered, the depth of the equivalent dislocation model, or D_{glock}, corresponds to locations creeping with velocities between $0.5V_{pl}$ and $0.62V_{pl}$, explaining why our models tend to such values in the late interseismic period. For example, the profile for M4 is nearly symmetric in the late interseismic period, and hence, D_{glock} corresponds to the depth with creep velocities of $0.5V_{pl}$. Note that the transition for M4 is similar in shape to that of a constant stress drop crack model at the top of the transition zone but deviates at greater depths. However, in models with smaller postseismic slip, such as M4-H, the profile at the bottom of the transition becomes more similar to that of the constant stress drop crack model, and hence, the D_{glock} corresponds to locations with higher creeping rates, closer to $0.62V_{pl}$ (Figure A2).

Appendix B: Locked-Creeping Transition on a Fault With Reduced Postseismic Slip

We consider a fault model similar to M4, except that its normal stress is increased from 50 MPa to the higher level, 330 MPa, at depths beyond 20 km, in order to reduce postseismic slip and explore its effect on the behavior of the locked-creeping transition zone (Figure B1). Note that 330 MPa corresponds to the lithostatic overburden minus hydrostatic pore pressure at 20 km depth. In this model, due to the increased $(a - b)\bar{\sigma}$, the induced postseismic slip transient is smaller in amplitude and extent, compared to model M4, leading to higher interseismic velocities in the late interseismic period (Figure B1a). The time evolution of $D_{0.1}$, $D_{0.5}$, and $D_{0.9}$ shows the same qualitative trends as in all other models M1 – M4, M4-L, and M4-H (Figure B1b). However, the transition zone is narrower than in the other models and $D_{0.9}$ is far from reaching the bottom of the simulated VS region, illustrating that this artifact in models M2 – M4 is qualitatively unimportant to the overall conclusions. Despite the fact that in this model, the postseismic slip is relatively minimal (Figure B1c, approximately the space between the second from the left red line and the first from the left blue line, minus the long-term creeping with V_{pl}), D_{glock} is still below D_{rupt} in the late interseismic period. As discussed in the main text, in the scenario with no postseismic slip, D_{rupt} would be deeper than D_{glock}, since the fault regions below D_{rupt} would have to slip with the long-term slip rate V_{pl}, and any interseismic slip penetrating up into the seismically ruptured domain would make D_{glock} shallower than D_{glock}. The example of this appendix shows that such a scenario would require atypical values of effective normal stress and/or friction properties.

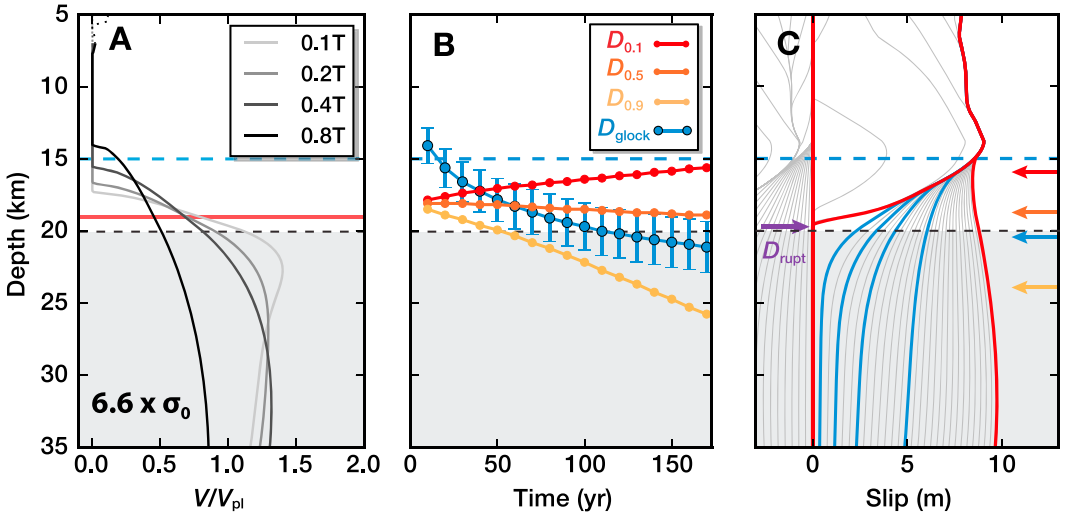

Figure B1. A fault model with increased normal stress and hence reduced postseismic slip at depth below 20 km. (a) The depth profile of normalized slip rates at different times of an interseismic period, with plotting conventions as in Figure 6. (b) Time evolution of $D_{0.1}$, $D_{0.5}$, $D_{0.9}$, and D_{glock}, with plotting conventions as in Figure 7. (c) Depth distribution of fault slip during the interseismic period, with plotting conventions as in Figure 11. The gray areas below the black dashed lines indicate fault areas with increased normal stress ($6.6\sigma_0$ = 330 MPa). Blue dashed lines mark the downdip VW/VS transition; red line marks the depth limit of DW.

Acknowledgments
This study was supported by the United States Geological Survey (grants G14AP00033 and G16AP00117), National Science Foundation (grants EAR 1142183 and 1520907), and the Southern California Earthquake Center (SCEC, funded by NSF Cooperative Agreement EAR-1033462 and USGS Cooperative Agreement G12AC20038). This is SCEC contribution 7171. J.J. was also supported by a Green Foundation Postdoctoral Fellowship in the Institute of Geophysics and Planetary Physics, Scripps Institution of Oceanography, University of California, San Diego. We thank Pablo Ampuero, Jean-Philippe Avouac, Tom Heaton, and Mark Simons for helpful discussions and comments on an earlier draft of the manuscript. We thank Yuri Fialko and David Sandwell for discussions on the topic. Numerical data are available upon request to the authors.

References

Ader, T. J., et al. (2012), Convergence rate across the Nepal Himalaya and interseismic coupling on the Main Himalayan Thrust: Implications for seismic hazard, *J. Geophys. Res.*, *117*, B04403, doi:10.1029/2011JB009071.

Akçiz, S. O., L. G. Ludwig, J. R. Arrowsmith, and O. Zielke (2010), Century-long average time intervals between earthquake ruptures of the San Andreas fault in the Carrizo Plain, California, *Geology*, *38*(9), 787–790, doi:10.1130/G30995.1.

Allam, A. A., and Y. Ben-Zion (2012), Seismic velocity structures in the southern California plate-boundary environment from double-difference tomography, *Geophys. J. Int.*, *190*(2), 1181–1196, doi:10.1111/j.1365-246x.2012.05544.x.

Allmann, B. P., and P. M. Shearer (2009), Global variations of stress drop for moderate to large earthquakes, *J. Geophys. Res.*, *114*, B01310, doi:10.1029/2008JB005821.

Ampuero, J.-P., and A. M. Rubin (2008), Earthquake nucleation on rate and state faults—Aging and slip laws, *J. Geophys. Res.*, *113*, B01302, doi:10.1029/2007JB005082.

Avouac, J.-P., L. Meng, S. Wei, T. Wang, and J.-P. Ampuero (2015), Lower edge of locked main himalayan thrust unzipped by the 2015 gorkha earthquake, *Nat. Geosci.*, *8*(9), 708–711.

Barbot, S., Y. Fialko, and Y. Bock (2009), Postseismic deformation due to the M_w 6.0 2004 Parkfield earthquake: Stress-driven creep on a fault with spatially variable rate-and-state friction parameters, *J. Geophys. Res.*, *114*, B07405, doi:10.1029/2008JB005748.

Barbot, S., N. Lapusta, and J.-P. Avouac (2012), Under the hood of the earthquake machine: Toward predictive modeling of the seismic cycle, *Science*, *336*(6082), 707–710, doi:10.1126/science.1218796.

Bayes, M., and M. Price (1763), An essay towards solving a problem in the doctrine of chances. by the late rev. Mr. Bayes, F. R. S. communicated by Mr. Price, in a letter to John Canton, A. M. F. R. S., *Philos. Trans.*, *53*, 370–418, doi:10.1098/rstl.1763.0053.

Ben-Zion, Y., and V. Lyakhovsky (2006), Analysis of aftershocks in a lithospheric model with seismogenic zone governed by damage rheology, *Geophys. J. Int.*, *165*(1), 197–210, doi:10.1111/j.1365-246x.2006.02878.x.

Ben-Zion, Y., and J. R. Rice (1995), Slip patterns and earthquake populations along different classes of faults in elastic solids, *J. Geophys. Res.*, *100*(B7), 12,959–12,983, doi:10.1029/94JB03037.

Ben-Zion, Y., and J. R. Rice (1997), Dynamic simulations of slip on a smooth fault in an elastic solid, *J. Geophys. Res.*, *102*(B8), 17,771–17,784, doi:10.1029/97JB01341.

Blanpied, M. L., D. A. Lockner, and J. D. Byerlee (1995), Frictional slip of granite at hydrothermal conditions, *J. Geophys. Res.*, *100*(B7), 13,045–13,064.

Bouchon, M., M. N. Toksöz, and H. Karabulut (2002), Space and time evolution of rupture and faulting during the 1999 İzmit (Turkey) earthquake, *Bull. Seismol. Soc. Am.*, *92*, 256–266.

Bruhat, L., S. Barbot, and J.-P. Avouac (2011), Evidence for postseismic deformation of the lower crust following the 2004 M_w 6.0 Parkfield earthquake, *J. Geophys. Res.*, *116*, B08401, doi:10.1029/2010JB008073.

Brune, J. N., T. L. Henyey, and R. F. Roy (1969), Heat flow, stress, and rate of slip along the San Andreas Fault, California, *J. Geophys. Res.*, *74*(15), 3821–3827, doi:10.1029/JB074i015p03821.

Bürgmann, R., and G. Dresen (2008), Rheology of the lower crust and upper mantle: Evidence from rock mechanics, geodesy, and field observations, *Annu. Rev. Earth Planet. Sci.*, *36*, 531–567.

Bürgmann, R., M. G. Kogan, G. M. Steblov, G. Hilley, V. E. Levin, and E. Apel (2005), Interseismic coupling and asperity distribution along the Kamchatka subduction zone, *J. Geophys. Res.*, *110*, B07405, doi:10.1029/2005JB003648.

Chang, S.-H., J.-P. Avouac, S. Barbot, and J.-C. Lee (2013), Spatially variable fault friction derived from dynamic modeling of aseismic afterslip due to the 2004 Parkfield earthquake, *J. Geophys. Res. Solid Earth*, *118*, 3431–3447, doi:10.1002/jgrb.50231.

Chen, Q., and J. T. Freymueller (2002), Geodetic evidence for a near-fault compliant zone along the San Andreas fault in the San Francisco bay area, *Bull. Seismol. Soc. Am.*, *92*(2), 656–671, doi:10.1785/0120010110.

Chen, T., and N. Lapusta (2009), Scaling of small repeating earthquakes explained by interaction of seismic and aseismic slip in a rate and state fault model, *J. Geophys. Res.*, *114*, B01311, doi:10.1029/2008JB005749.
Chester, F. M., and J. S. Chester (1998), Ultracataclasite structure and friction processes of the Punchbowl fault, San Andreas system, California, *Tectonophysics*, *295*(1–2), 199–221.
Chuang, R. Y., and K. M. Johnson (2011), Reconciling geologic and geodetic model fault slip-rate discrepancies in Southern California: Consideration of nonsteady mantle flow and lower crustal fault creep, *Geology*, *39*(7), 627–630, doi:10.1130/G32120.1.
Cochran, E. S., Y.-G. Li, P. M. Shearer, S. Barbot, Y. Fialko, and J. E. Vidale (2009), Seismic and geodetic evidence for extensive, long-lived fault damage zones, *Geology*, *37*(4), 315–318, doi:10.1130/G25306A.1.
Cole, J., B. R. Hacker, L. Ratschbacher, J. F. Dolan, G. Seward, C. Frohlich, and W. Frank (2007), Localized ductile shear below the seismogenic zone: Structural analysis of an exhumed strike-slip fault, Austrian Alps, *J. Geophys. Res.*, *112*, B12304, doi:10.1029/2007JB004975.
Cubas, N., N. Lapusta, J.-P. Avouac, and H. Perfettini (2015), Numerical modeling of long-term earthquake sequences on the NE Japan megathrust: Comparison with observations and implications for fault friction, *Earth Planet. Sci. Lett.*, *419*, 1–12, doi:10.1016/j.epsl.2015.03.002.
Das, S., and C. H. Scholz (1983), Why large earthquakes do not nucleate at shallow depths, *Nature*, *141*(3), 183–206, doi:10.1016/j.pepi.2003.11.002.
Day, S. M., L. A. Dalguer, and N. Lapusta (2005), Comparison of finite difference and boundary integral solutions to three-dimensional spontaneous rupture, *J. Geophys. Res.*, *110*, B12307, doi:10.1029/2005JB003813.
DeVries, P. M. R., and B. J. Meade (2016), Kinematically consistent models of viscoelastic stress evolution, *Geophys. Res. Lett.*, *43*, 4205–4214, doi:10.1002/2016GL068375.
Di Toro, G., R. Han, T. Hirose, N. De Paola, S. Nielsen, K. Mizoguchi, F. Ferri, M. Cocco, and T. Shimamoto (2011), Fault lubrication during earthquakes, *Nature*, *471*(7339), 494–498, doi:10.1038/nature09838.
Dieterich, J. (2007), Applications of rate- and state-dependent friction to models of fault-slip and earthquake occurrence, in *Treatise on Geophysics*, 2nd, edited by G. Schubert, pp. 93–110, Elsevier, Oxford, doi:10.1016/B978-0-444-53802-4.00075-0.
Dieterich, J. H. (1979), Modeling of rock friction. 1. Experimental results and constitutive equations, *J. Geophys. Res.*, *84*(NB5), 2161–2168, doi:10.1029/JB084iB05p02161.
Dieterich, J. H. (1981), Potential for geophysical experiments in large scale tests, *Geophys. Res. Lett.*, *8*(7), 653–656, doi:10.1029/GL008i007p00653/pdf.
Doser, D. I., and H. Kanamori (1986), Depth of seismicity in the Imperial Valley region (1977–1983) and its relationship to heat flow, crustal structure, and the October 15, 1979, earthquake, *J. Geophys. Res.*, *91*, 675–688.
Dragert, H., K. Wang, and T. S. James (2001), A silent slip event on the deeper Cascadia subduction interface, *Science*, *292*(5521), 1525–1528, doi:10.1126/science.1060152.
Dublanchet, P., P. Bernard, and P. Favreau (2013), Interactions and triggering in a 3-D rate-and-state asperity model, *J. Geophys. Res. Solid Earth*, *118*, 2225–2245, doi:10.1002/jgrb.50187.
Duputel, Z., P. S. Agram, M. Simons, S. E. Minson, and J. L. Beck (2014), Accounting for prediction uncertainty when inferring subsurface fault slip, *Geophys. J. Int.*, *197*(1), 464–482, doi:10.1093/gji/ggt517.
Eberhart-Phillips, D., et al. (2003), The 2002 Denali fault earthquake, Alaska: A large magnitude, slip-partitioned event, *Science*, *300*(5622), 1113–1118, doi:10.1126/science.1082703.
Eshelby, J. D. (1957), The determination of the elastic field of an ellipsoidal inclusion, and related problems, *Proc. R. Soc. London, Ser. A*, *241*(1226), 376–396, doi:10.1098/rspa.1957.0133.
Fialko, Y. (2006), Interseismic strain accumulation and the earthquake potential on the southern San Andreas fault system, *Nature*, *441*(7096), 968–971, doi:10.1038/nature04797.
Fialko, Y., D. Sandwell, D. Agnew, M. Simons, P. Shearer, and B. Minster (2002), Deformation on nearby faults induced by the 1999 Hector Mine earthquake, *Science*, *297*(5588), 1858–1862, doi:10.1126/science.1074671.
Fialko, Y., D. Sandwell, M. Simons, and P. Rosen (2005), Three-dimensional deformation caused by the Bam, Iran, earthquake and the origin of shallow slip deficit, *Nature*, *435*(7040), 295–299.
Grant, L. B., and A. Donnellan (1994), 1855 and 1991 surveys of the San Andreas fault: Implications for fault mechanics, *Bull. Seismol. Soc. Am.*, *84*(2), 241–246.
Hauksson, E. (2010), Spatial separation of large earthquakes, aftershocks, and background seismicity: Analysis of interseismic and coseismic seismicity patterns in Southern California, *Pure Appl. Geophys.*, *167*(8), 979–997, doi:10.1007/s00024-010-0083-3.
Hauksson, E., W. Yang, and P. M. Shearer (2012), Waveform relocated earthquake catalog for Southern California (1981 to June 2011), *Bull. Seismol. Soc. Am.*, *102*(5), 2239–2244, doi:10.1785/0120120010.
Hearn, E. H., R. Bürgmann, and R. E. Reilinger (2002), Dynamics of İzmit earthquake postseismic deformation and loading of the Düzce earthquake hypocenter, *Bull. Seismol. Soc. Am.*, *92*(1), 172–193, doi:10.1785/0120000832.
Henstock, T. J., A. Levander, and J. A. Hole (1997), Deformation in the lower crust of the San Andreas fault system in Northern California, *Science*, *278*(5338), 650–653, doi:10.1126/science.278.5338.650.
Hetland, E. A., and M. Simons (2010), Post-seismic and interseismic fault creep II: Transient creep and interseismic stress shadows on megathrusts, *Geophys. J. Int.*, *181*(1), 99–112, doi:10.1111/j.1365-246x.2009.04482.x.
Hetland, E. A., M. Simons, and E. M. Dunham (2010), Post-seismic and interseismic fault creep I: Model description, *Geophys. J. Int.*, *181*(1), 81–98, doi:10.1111/j.1365-246x.2010.04522.x.
Hillers, G., Y. Ben-Zion, and P. M. Mai (2006), Seismicity on a fault controlled by rate- and state-dependent friction with spatial variations of the critical slip distance, *J. Geophys. Res.*, *111*, B01403, doi:10.1029/2005JB003859.
Hillers, G., P. M. Mai, Y. Ben-Zion, and J.-P. Ampuero (2007), Statistical properties of seismicity of fault zones at different evolutionary stages, *Geophys. J. Int.*, *169*(2), 515–533, doi:10.1111/j.1365-246x.2006.03275.x.
Hori, T., N. Kato, K. Hirahara, T. Baba, and Y. Kaneda (2004), A numerical simulation of earthquake cycles along the Nankai Trough in southwest Japan: Lateral variation in frictional property due to the slab geometry controls the nucleation position, *Earth Planet. Sci. Lett.*, *228*(3–4), 215–226, doi:10.1016/j.epsl.2004.09.033.
Jiang, J., and Y. Fialko (2016), Reconciling seismicity and geodetic locking depths on the Anza section of the San Jacinto fault, *Geophys. Res. Lett.*, *43*, 10,663–10,671, doi:10.1002/2016GL071113.
Jiang, J., and N. Lapusta (2015), Variability of earthquake slip and arresting depth in fault models with depth-dependent properties, paper presented at SSA 2015 Annual Meeting, Pasadena, Calif.
Jiang, J., and N. Lapusta (2016), Deeper penetration of large earthquakes on seismically quiescent faults, *Science*, *352*(6291), 1293–1297, doi:10.1126/science.aaf1496.

Johnson, K. M., and P. Segall (2004), Viscoelastic earthquake cycle models with deep stress-driven creep along the San Andreas fault system, *J. Geophys. Res.*, *109*, B10403, doi:10.1029/2004JB003096.
Johnson, K. M., R. Bürgmann, and K. Larson (2006), Frictional properties on the San Andreas Fault near Parkfield, California, inferred from models of afterslip following the 2004 earthquake, *Bull. Seismol. Soc. Am.*, *96*(4B), S321—S338, doi:10.1785/0120050808.
Johnson, K. M., R. Bürgmann, and J. T. Freymueller (2009), Coupled afterslip and viscoelastic flow following the 2002 Denali Fault, Alaska earthquake, *Geophys. J. Int.*, *176*(3), 670–682, doi:10.1111/j.1365-246x.2008.04029.x.
Jolivet, R., R. Bürgmann, and N. Houlié (2009), Geodetic exploration of the elastic properties across and within the northern San Andreas Fault zone, *Earth Planet. Sci. Lett.*, *288*(1–2), 126–131, doi:10.1016/j.epsl.2009.09.014.
Kagan, Y. Y., D. D. Jackson, and Y. Rong (2006), A new catalog of southern California earthquakes, 1800–2005, *Seismol. Res. Lett.*, *77*(1), 30–38, doi:10.1785/gssrl.77.1.30.
Kanamori, H., and D. Hadley (1975), Crustal structure and temporal velocity change in Southern California, *Pure. Appl. Geophys.*, *113*(1), 257–280, doi:10.1007/BF01592916.
Kaneko, Y., and N. Lapusta (2008), Variability of earthquake nucleation in continuum models of rate-and-state faults and implications for aftershock rates, *J. Geophys. Res.*, *113*, B12312, doi:10.1029/2007JB005154.
Kaneko, Y., and N. Lapusta (2010), Supershear transition due to a free surface in 3-D simulations of spontaneous dynamic rupture on vertical strike-slip faults, *Tectonophysics*, *493*(3–4), 272–284, doi:10.1016/j.tecto.2010.06.015.
Kaneko, Y., J.-P. Avouac, and N. Lapusta (2010), Towards inferring earthquake patterns from geodetic observations of interseismic coupling, *Nat. Geosci.*, *3*(5), 363–369, doi:10.1038/ngeo843.
Kato, N. (2004), Interaction of slip on asperities: Numerical simulation of seismic cycles on a two-dimensional planar fault with nonuniform frictional property, *J. Geophys. Res.*, *109*, B12306, doi:10.1029/2004JB003001.
Lachenbruch, A. H. (1980), Frictional heating, fluid pressure, and the resistance to fault motion, *J. Geophys. Res.*, *85*(B11), 6097–6112, doi:10.1029/JB085iB11p06097.
Lambert, V., and S. Barbot (2016), Contribution of viscoelastic flow in earthquake cycles within the lithosphere-asthenosphere system, *Geophys. Res. Lett.*, *43*, 10,142–10,154, doi:10.1002/2016GL070345.
Lapusta, N., and Y. Liu (2009), Three-dimensional boundary integral modeling of spontaneous earthquake sequences and aseismic slip, *J. Geophys. Res.*, *114*, B09303, doi:10.1029/2008JB005934.
Lapusta, N., and J. R. Rice (2003), Nucleation and early seismic propagation of small and large events in a crustal earthquake model, *J. Geophys. Res.*, *108*, 2205, doi:10.1029/2001JB000793.
Lapusta, N., J. R. Rice, Y. Ben-Zion, and G. Zheng (2000), Elastodynamic analysis for slow tectonic loading with spontaneous rupture episodes on faults with rate- and state-dependent friction, *J. Geophys. Res.*, *105*, 23,765–23,789.
Lay, T., H. Kanamori, C. J. Ammon, K. D. Koper, A. R. Hutko, L. Ye, H. Yue, and T. M. Rushing (2012), Depth-varying rupture properties of subduction zone megathrust faults, *J. Geophys. Res.*, *117*, B04311, doi:10.1029/2011JB009133.
Li, V. C., and J. R. Rice (1987), Crustal deformation in great California earthquake cycles, *J. Geophys. Res.*, *92*(B11), 11,533–11,551.
Lin, G., P. M. Shearer, and E. Hauksson (2007), Applying a three-dimensional velocity model, waveform cross correlation, and cluster analysis to locate Southern California seismicity from 1981 to 2005, *J. Geophys. Res.*, *112*, B12309, doi:10.1029/2007JB004986.
Lindsey, E. O., and Y. Fialko (2013), Geodetic slip rates in the southern San Andreas Fault System: Effects of elastic heterogeneity and fault geometry, *J. Geophys. Res. Solid Earth*, *118*, 689–697, doi:10.1029/2012JB009358.
Lindsey, E. O., V. J. Sahakian, Y. Fialko, Y. Bock, S. Barbot, and T. K. Rockwell (2013), Interseismic strain localization in the San Jacinto Fault Zone, *Pure. Appl. Geophys.*, *171*(11), 2937–2954, doi:10.1007/s00024-013-0753-z.
Lindsey, E. O., Y. Fialko, Y. Bock, D. T. Sandwell, and R. Bilham (2014), Localized and distributed creep along the southern San Andreas Fault, *J. Geophys. Res. Solid Earth*, *119*, 7909–7922, doi:10.1002/2014JB011275.
Liu, Y., and J. R. Rice (2005), Aseismic slip transients emerge spontaneously in three-dimensional rate and state modeling of subduction earthquake sequences, *J. Geophys. Res.*, *110*, B08307, doi:10.1029/2004JB003424.
Liu, Y., and J. R. Rice (2007), Spontaneous and triggered aseismic deformation transients in a subduction fault model, *J. Geophys. Res.*, *112*, B09404, doi:10.1029/2007JB004930.
Liu, Y., and A. M. Rubin (2010), Role of fault gouge dilatancy on aseismic deformation transients, *J. Geophys. Res.*, *115*, B10414, doi:10.1029/2010JB007522.
Lyakhovsky, V., Y. Ben-Zion, and A. Agnon (2001), Earthquake cycle, fault zones, and seismicity patterns in a rheologically layered lithosphere, *J. Geophys. Res.*, *106*, 4103–4120.
Marone, C. J., C. H. Scholz, and R. Bilham (1991), On the mechanics of earthquake afterslip, *J. Geophys. Res.*, *96*(B5), 8441–8452, doi:10.1029/91JB00275.
Materna, K., and R. Bürgmann (2016), Contrasts in compliant fault zone properties inferred from geodetic measurements in the San Francisco bay area, *J. Geophys. Res. Solid Earth*, *121*, 6916–6931, doi:10.1002/2016JB013243.
Mavrommatis, A. P., P. Segall, and K. M. Johnson (2014), A decadal-scale deformation transient prior to the 2011 M_w 9.0 Tohoku-oki earthquake, *Geophys. Res. Lett.*, *41*, 4486–4494, doi:10.1002/2014GL060139.
Mavrommatis, A. P., P. Segall, N. Uchida, and K. M. Johnson (2015), Long-term acceleration of aseismic slip preceding the M_w 9 Tohoku-oki earthquake: Constraints from repeating earthquakes, *Geophys. Res. Lett.*, *42*, 9717–9725, doi:10.1002/2015GL066069.
Meade, B. J. (2005), Block models of crustal motion in southern California constrained by GPS measurements, *J. Geophys. Res.*, *110*, B03403, doi:10.1029/2004JB003209.
Meade, B. J., and B. H. Hager (2004), Viscoelastic deformation for a clustered earthquake cycle, *Geophys. Res. Lett.*, *31*, L10610, doi:10.1029/2004GL019643.
Mitchell, E. K., Y. Fialko, and K. M. Brown (2016), Velocity-weakening behavior of westerly granite at temperature up to 600°C, *J. Geophys. Res. Solid Earth*, *121*, 6932–6946, doi:10.1002/2016JB013081.
Nadeau, R. M., and L. R. Johnson (1998), Seismological studies at Parkfield VI: Moment release rates and estimates of source parameters for small repeating earthquakes, *Bull. Seismol. Soc. Am.*, *88*(3), 790–814.
Nazareth, J. J., and E. Hauksson (2004), The seismogenic thickness of the Southern California crust, *Bull. Seismol. Soc. Am.*, *94*(3), 940–960.
Noda, H., and N. Lapusta (2010), Three-dimensional earthquake sequence simulations with evolving temperature and pore pressure due to shear heating: Effect of heterogeneous hydraulic diffusivity, *J. Geophys. Res.*, *115*, B12314, doi:10.1029/2010JB007780.
Noda, H., and N. Lapusta (2013), Stable creeping fault segments can become destructive as a result of dynamic weakening, *Nature*, *493*(7433), 518–521, doi:10.1038/nature11703.
Noda, H., and T. Shimamoto (2005), Thermal pressurization and slip-weakening distance of a fault: An example of the Hanaore fault, southwest Japan, *Bull. Seismol. Soc. Am.*, *95*(4), 1224–1233.

Noda, H., and T. Shimamoto (2010), A rate- and state-dependent ductile flow law of polycrystalline halite under large shear strain and implications for transition to brittle deformation, *Geophys. Res. Lett.*, *37*, L09310, doi:10.1029/2010GL042512.
Noda, H., N. Lapusta, and H. Kanamori (2013), Comparison of average stress drop measures for ruptures with heterogeneous stress change and implications for earthquake physics, *Geophys. J. Int.*, *193*(3), 1691–1712, doi:10.1093/gji/ggt074.
Nur, A., and G. Mavko (1974), Postseismic viscoelastic rebound, *Science*, *183*(4121), 204–206, doi:10.1126/science.183.4121.204.
Onderdonk, N. W., S. F. McGill, and T. K. Rockwell (2015), Short-term variations in slip rate and size of prehistoric earthquakes during the past 2000 years on the northern San Jacinto fault zone, a major plate-boundary structure in southern California, *Lithosphere*, *7*(3), 211–234, doi:10.1130/L393.1.
Palmer, A., and J. R. Rice (1973), The growth of slip surfaces in the progressive failure of over-consolidated clay, *Proc. R. Soc. London, Ser. B*, *332*(1591), 527–548.
Parsons, T. (1998), Seismic-reflection evidence that the Hayward fault extends into the lower crust of the San Francisco bay area, California, *Bull. Seismol. Soc. Am.*, *88*(5), 1212–1223.
Patil, A., D. Huard, and C. Fonnesbeck (2010), PyMC: Bayesian stochastic modelling in python, *J. Stat. Softw.*, *35*(1), 1–81, doi:10.18637/jss.v035.i04.
Perfettini, H., and J.-P. Ampuero (2008), Dynamics of a velocity strengthening fault region: Implications for slow earthquakes and postseismic slip, *J. Geophys. Res.*, *113*, B09411, doi:10.1029/2007JB005398.
Perfettini, H., and J. P. Avouac (2007), Modeling afterslip and aftershocks following the 1992 Landers earthquake, *J. Geophys. Res.*, *112*, B07409, doi:10.1029/2006JB004399.
Philibosian, B., T. E. Fumal, and R. Weldon (2011), San Andreas fault earthquake chronology and Lake Cahuilla history at Coachella, California, *Bull. Seismol. Soc. Am.*, *101*(1), 13–38, doi:10.1785/0120100050.
Platt, J., B. Proctor, T. Mitchell, G. Hirth, D. Goldsby, G. Di Toro, N. Beeler, and T. Tullis (2015), The role of gouge and temperature on flash heating and its hysteresis, in *EGU General Assembly Conference Abstracts*, vol. 17, p. 7787, EGU, Vienna.
Platt, J. D., J. W. Rudnicki, and J. R. Rice (2014), Stability and localization of rapid shear in fluid-saturated fault gouge: 2. Localized zone width and strength evolution, *J. Geophys. Res. Solid Earth*, *119*, 4334–4359, doi:10.1002/2013JB010711.
Plesch, A., et al. (2007), Community Fault Model (CFM) for Southern California, *Bull. Seismol. Soc. Am.*, *97*(6), 1793–1802, doi:10.1785/0120050211.
Reilinger, R. E., S. Ergintav, R. Burgmann, and S. McClusky (2000), Coseismic and postseismic fault slip for the 17 August 1999, $M = 7.5$, İzmit, Turkey earthquake, *Science*, *289*(5484), 1519–1524, doi:10.1126/science.289.5484.1519.
Rice, J. R. (1992), Fault stress states, pore pressure distributions, and the weakness of the San Andreas fault, *Int. Geophys. Ser.*, *51*, 3–521.
Rice, J. R. (1993), Spatio-temporal complexity of slip on a fault, *J. Geophys. Res.*, *98*(B6), 9885–9907.
Rice, J. R. (2006), Heating and weakening of faults during earthquake slip, *J. Geophys. Res.*, *111*, B05311, doi:10.1029/2005JB004006.
Rice, J. R., and A. L. Ruina (1983), Stability of steady frictional slipping, *J. Appl. Mech. T. ASME*, *50*(2), 343–349.
Rockwell, T. K., T. E. Dawson, J. Y. Ben-Horin, and G. Seitz (2015), A 21-event, 4,000-year history of surface ruptures in the Anza seismic gap, San Jacinto fault, and implications for long-term earthquake production on a major plate boundary fault, *Pure. Appl. Geophys.*, *172*(5), 1143–1165, doi:10.1007/s00024-014-0955-z.
Rolandone, F., R. Bürgmann, and R. M. Nadeau (2004), The evolution of the seismic-aseismic transition during the earthquake cycle: Constraints from the time-dependent depth distribution of aftershocks, *Geophys. Res. Lett.*, *31*, L23610, doi:10.1029/2004GL021379.
Rousset, B., S. Barbot, J.-P. Avouac, and Y.-J. Hsu (2012), Postseismic deformation following the 1999 Chi-Chi earthquake, Taiwan: Implication for lower-crust rheology, *J. Geophys. Res.*, *117*, B12405, doi:10.1029/2012JB009571.
Ruina, A. (1983), Slip instability and state variable friction laws, *J. Geophys. Res.*, *88*(B12), 10,359–10,370, doi:10.1029/JB088iB12p10359.
Runnerstrom, E. E., L. B. Grant, J. R. Arrowsmith, D. D. Rhodes, and E. M. Stone (2002), Displacement across the Cholame segment of the San Andreas fault between 1855 and 1893 from cadastral surveys, *Bull. Seismol. Soc. Am.*, *92*(7), 2659–2669, doi:10.1785/0120000603.
Savage, J. C. (1990), Equivalent strike-slip earthquake cycles in half-space and lithosphere-asthenosphere earth models, *J. Geophys. Res.*, *95*(B4), 4873–4879, doi:10.1029/JB095iB04p04873.
Savage, J. C., and R. O. Burford (1973), Geodetic determination of relative plate motion in central California, *J. Geophys. Res.*, *78*(5), 832–845, doi:10.1029/JB078i005p00832/pdf.
Savage, J. C., and W. H. Prescott (1978), Asthenosphere readjustment and the earthquake cycle, *J. Geophys. Res.*, *83*(B7), 3369–3376, doi:10.1029/JB083iB07p03369.
Schaff, D. P., G. Bokelmann, G. C. Beroza, F. Waldhauser, and W. L. Ellsworth (2002), High-resolution image of Calaveras Fault seismicity, *J. Geophys. Res.*, *107*, 5–16, doi:10.1029/2001JB000633.
Scholz, C. H. (1998), Earthquakes and friction laws, *Nature*, *391*(6662), 37–42.
Schwartz, S. Y., and J. M. Rokosky (2007), Slow slip events and seismic tremor at circum-Pacific subduction zones, *Rev. Geophys.*, *45*, RG3004, doi:10.1029/2006RG000208.
Segall, P. (2002), Integrating geologic and geodetic estimates of slip rate on the San Andreas fault system, *Int. Geol. Rev.*, *44*(1), 62–82, doi:10.2747/0020-6814.44.1.62.
Segall, P. (2010), *Earthquake and Volcano Deformation*, Princeton Univ. Press, Princeton, N. J.
Segall, P., A. M. Rubin, A. M. Bradley, and J. R. Rice (2010), Dilatant strengthening as a mechanism for slow slip events, *J. Geophys. Res.*, *115*, B12305, doi:10.1029/2010JB007449.
Shaw, B. E., and J. R. Rice (2000), Existence of continuum complexity in the elastodynamics of repeated fault ruptures, *J. Geophys. Res.*, *105*, 23,791–23,810, doi:10.1029/2000JB900203.
Shelly, D. R. (2010), Migrating tremors illuminate complex deformation beneath the seismogenic San Andreas fault, *Nature*, *463*(7281), 648–U75, doi:10.1038/nature08755.
Shibazaki, B., and Y. Iio (2003), On the physical mechanism of silent slip events along the deeper part of the seismogenic zone, *Geophys. Res. Lett.*, *30*(9), 1489, doi:10.1029/2003GL017047.
Shimamoto, T., and H. Noda (2014), A friction to flow constitutive law and its application to a 2-D modeling of earthquakes, *J. Geophys. Res. Solid Earth*, *119*(11), 8089–8106, doi:10.1002/2014JB011170.
Sibson, R. H. (1973), Interactions between temperature and pore-fluid pressure during earthquake faulting and a mechanism for partial or total stress relief, *Nature*, *243*(126), 66–68.
Sibson, R. H. (1982), Fault zone models, heat flow, and the depth distribution of earthquakes in the continental crust of the United States, *Bull. Seismol. Soc. Am.*, *72*(1), 151–163.
Sibson, R. H. (1984), Roughness at the base of the seismogenic zone: Contributing factors, *J. Geophys. Res.*, *89*(B7), 5791–5799.
Sibson, R. H. (2014), Earthquake rupturing in fluid-overpressured crust: How common?, *Pure Appl. Geophys.*, *171*(11), 2867–2885, doi:10.1007/s00024-014-0838-3.

Sieh, K. E. (1978), Slip along the San Andreas fault associated with the great 1857 earthquake, *Bull. Seismol. Soc. Am.*, *68*(5), 1421–1448.
Sieh, K. E., and P. L. Williams (1990), Behavior of the southernmost San Andreas Fault during the past 300 years, *J. Geophys. Res.*, *95*(B5), 6629–6645, doi:10.1029/JB095iB05p06629.
Simons, M., Y. Fialko, and L. Rivera (2002), Coseismic deformation from the 1999 M_w 7.1 Hector Mine, California, earthquake as inferred from InSAR and GPS observations, *Bull. Seismol. Soc. Am.*, *92*(4), 1390–1402, doi:10.1785/0120000933.
Simons, M., et al. (2011), The 2011 magnitude 9.0 Tohoku-oki earthquake: Mosaicking the megathrust from seconds to centuries, *Science*, *332*(6036), 1421–1425.
Smith, B., and D. Sandwell (2004), A three-dimensional semianalytic viscoelastic model for time-dependent analyses of the earthquake cycle, *J. Geophys. Res.*, *109*, B12401, doi:10.1029/2004JB003185.
Smith, B. R., and D. T. Sandwell (2006), A model of the earthquake cycle along the San Andreas Fault System for the past 1000 years, *J. Geophys. Res.*, *111*, B01405, doi:10.1029/2005JB003703.
Smith-Konter, B. R., D. T. Sandwell, and P. M. Shearer (2011), Locking depths estimated from geodesy and seismology along the San Andreas Fault System: Implications for seismic moment release, *J. Geophys. Res.*, *116*, B06401, doi:10.1029/2010JB008117.
Stevens, V. L., and J. P. Avouac (2015), Interseismic coupling on the main Himalayan thrust, *Geophys. Res. Lett.*, *42*(14), 5828–5837, doi:10.1002/2015GL064845.
Suppe, J. (2014), Fluid overpressures and strength of the sedimentary upper crust, *J. Struct. Geol.*, *69*, 481–492, doi:10.1016/j.jsg.2014.07.009.
Takeuchi, C. S., and Y. Fialko (2012), Dynamic models of interseismic deformation and stress transfer from plate motion to continental transform faults, *J. Geophys. Res.*, *117*, B05403, doi:10.1029/2011JB009056.
Takeuchi, C. S., and Y. Fialko (2013), On the effects of thermally weakened ductile shear zones on postseismic deformation, *J. Geophys. Res. Solid Earth*, *118*, 6295–6310, doi:10.1002/2013JB010215.
Thomas, M. Y., N. Lapusta, H. Noda, and J.-P. Avouac (2014), Quasi-dynamic versus fully dynamic simulations of earthquakes and aseismic slip with and without enhanced coseismic weakening, *J. Geophys. Res. Solid Earth*, *119*, 1986–2004, doi:10.1002/2013JB010615.
Thurber, C. H. (2006), Three-dimensional compressional wavespeed model, earthquake relocations, and focal mechanisms for the Parkfield, California, region, *Bull. Seismol. Soc. Am.*, *96*(4B), S38—S49, doi:10.1785/0120050825.
Tong, X., B. R. Smith-Konter, and D. T. Sandwell (2014), Is there a discrepancy between geological and geodetic slip rates along the San Andreas Fault System?, *J. Geophys. Res. Solid Earth*, *119*, 2518–2538, doi:10.1002/2013JB010765.
Tong, X., D. T. Sandwell, and B. Smith-Konter (2015), An integral method to estimate the moment accumulation rate on the Creeping Section of the San Andreas Fault, *Geophys. J. Int.*, *203*(1), 48–62, doi:10.1093/gji/ggv269.
Toppozada, T., and D. Branum (2002), California earthquakes of $M \leq 5.5$: Their history and the areas damaged, in *International Handbook of Earthquake and Engineering Seismology, Part A, International Geophysics*, vol. 81, edited by T. Toppozada and D. Branum, pp. 793–796, Academic Press, San Diego, Calif., doi:10.1016/S0074-6142(02)80252-2.
Tormann, T., S. Wiemer, and A. Mignan (2014), Systematic survey of high-resolution b value imaging along Californian faults: Inference on asperities, *J. Geophys. Res. Solid Earth*, *119*, 2029–2054, doi:10.1002/2013JB010867.
Townend, J., and M. D. Zoback (2004), Regional tectonic stress near the San Andreas fault in central and southern California, *Geophys. Res. Lett.*, *31*(15), L15S11, doi:10.1029/2003GL018918.
Tse, S. T., and J. R. Rice (1986), Crustal earthquake instability in relation to the depth variation of frictional slip properties, *J. Geophys. Res.*, *91*(B9), 9452–9472, doi:10.1029/JB091iB09p09452/full.
Tullis, T. (2015), Mechanisms for friction of rock at earthquake slip rates, in *Treatise on Geophysics*, 2nd, edited by G. Schubert, pp. 139–159, Elsevier, Oxford, doi:10.1016/B978-0-444-53802-4.00073-7.
Uchida, N., and T. Matsuzawa (2013), Pre-and postseismic slow slip surrounding the 2011 Tohoku-oki earthquake rupture, *Earth Planet. Sci. Lett.*, *374*, 81–91, doi:10.1016/j.epsl.2013.05.021.
Viesca, R. C., and D. I. Garagash (2015), Ubiquitous weakening of faults due to thermal pressurization, *Nature Geosci*, *8*(11), 875–879.
Waldhauser, F., and D. P. Schaff (2008), Large-scale relocation of two decades of Northern California seismicity using cross-correlation and double-difference methods, *J. Geophys. Res.*, *113*, B08311, doi:10.1029/2007JB005479.
Yue, H., et al. (2016), Depth varying rupture properties during the 2015 mw 7.8 gorkha (Nepal) earthquake, *Tectonophysics*, doi:10.1016/j.tecto.2016.07.005, in press.
Zhu, L. (2000), Crustal structure across the San Andreas Fault, Southern California from teleseismic converted waves, *Earth Planet. Sci. Lett.*, *179*(1), 183–190, doi:10.1016/S0012-821X(00)00101-1.
Zielke, O., J. R. Arrowsmith, L. G. Ludwig, and S. O. Akciz (2010), Slip in the 1857 and earlier large earthquakes along the Carrizo Plain, San Andreas fault, *Science*, *327*(5969), 1119–1122, doi:10.1126/science.1182781.